Journal of Sound and Vibration 636 (2026) 119799

Contents lists available at ScienceDirect

Journal of Sound and Vibration

journal homepage: www.elsevier.com/locate/jsvi

Contradirectional coupling and complete band gap formation in periodically folded beams and plates

Elisabetta Manconi [a,*], Filippo Dall'olio [a], Marco Riboli [b], Antonio Zippo [c], Farzad Tatar [a]

[a] Department of Industrial Engineering Systems and Technologies, University of Parma, Italy
[b] Department on Innovative Technologies, University of Applied Sciences and Arts of Southern Switzerland, SUPSI, Lugano, Switzerland
[c] Department of Engineering "Enzo Ferrari", University of Modena and Reggio Emilia, Italy

ARTICLE INFO

Keywords:
Folded structures
Band gap
Wave propagation
Periodic structures
Dynamic stiffness method (DSM)
Wave finite element method (WFE)

ABSTRACT

Periodic structures exhibit frequency ranges, known as band gaps, in which wave propagation is strongly attenuated due to Bragg scattering. In addition to this well-known mechanism, other band gaps can arise from wavemode coupling. This study investigates the contradirectional coupling between waves with opposite group velocities as a key mechanism for creating complete band gaps in periodically folded structures. Using the Dynamic Stiffness Method (DSM) and the Wave Finite Element (WFE) formulations, the analyses demonstrate how periodic folding couples flexural, longitudinal, and torsional wavemodes. Starting from the planar configuration, reference dispersion curves are used to identify critical points where the formation of the contradirectional coupling begins. A parametric study, supported by dispersion maps, identifies and quantifies the influence of geometric parameters on the position and width of the band gaps. WFE simulations show wavemode hybridisation by analysing energy distribution and visualising wavemode displacements near coupling and uncoupling points. The effects of modelling assumptions, such as finite thickness and fold curvature, are further studied, indicating that modelling simplifications can affect the hierarchy of wavemodes coupling and the edges of the band gaps. Experimental tests on a finite steel folded plate validate the numerical predictions, confirming the presence, location, and width of the contradirectional band gap.

1. Introduction

The control of elastic wave propagation in periodic and architected structures has attracted significant attention due to its importance in vibration attenuation, noise reduction, sensing, and energy harvesting applications [1–5]. Metamaterials have emerged as a rich field of research dedicated to controlling wave dispersion and creating band gaps - frequency ranges where waves cannot propagate - through two main mechanisms: periodicity and local resonance [6,7]. Periodicity results in the formation of Bragg band gaps, which occur when the wavelength becomes comparable to the lattice spacing [2,8], while locally resonant designs can generate tunable band gaps using embedded resonators that couple with the host structure [1,9]. Although effective, these mechanisms have inherent limitations for structural applications. Bragg scattering naturally occurs at high frequencies, related to the periodic length, making it unsuitable for low-frequency vibration control in structures; band gaps due to local resonators overcome this limitation but often require additional resonant masses or complex multi-material interfaces, increasing fabrication complexity and potentially

* Corresponding author.
E-mail address: elisabetta.manconi@unipr.it (E. Manconi).

https://doi.org/10.1016/j.jsv.2026.119799
Received 18 November 2025; Received in revised form 17 February 2026; Accepted 3 April 2026
Available online 8 April 2026

reducing structural efficiency [10,11]. These issues have motivated researchers to explore combined or alternative methods that can generate broad and tunable band gaps without extra resonant components [7].

An opportunity arises from wave coupling, which can lead to locking phenomena in the dispersion diagram related to coupling of wavemodes. The focus of this study is on wave coupling that occurs when counter-propagating waves with opposite group velocities interact and merge into a complex-conjugate pair. This mechanism of wave coupling, together with periodicity, can be utilised to create complete band gaps in which no wavemodes can propagate. Unlike periodicity or local resonances, it relies on intrinsic interactions between structural wavemodes and can be introduced through the geometry of the unit cell. As an example, Gao et al. [12] experimentally demonstrated that a V-folded acoustic black-hole beam exhibits ultra-wide complete band gaps below 1 kHz as a result of longitudinal-flexural coupling. Several other studies have reported similar behaviour in folded or corrugated structures, and a selection of these works is cited below. The concept of contradirectional coupling originates from optical and quantum systems; in optics, for instance, it was formalised within the framework of Coupled-Mode Theory (CMT) to describe interactions between counter-propagating wavemodes in optical waveguides and gratings, e.g., [13,14]. A contradirectional band gap describes the scenario in which two waves moving in opposite directions interact, creating a region of reduced standing energy. Such behaviour has mainly been observed and studied in devices like gratings and photonic crystals, where periodic structures easily cause forward- and backwards-propagating waves to interfere destructively, thus forming tunable filters. The term "contradirectional band gap" is used here in the context of structural wave dynamics to describe the frequency locking between waves propagating with opposite group velocities, which leads to the formation of a complete band gap.

The phenomenon has been reported in previous numerical and experimental studies. Friis and Ohlrich [15] demonstrated that periodically constrained beams with eccentric side branches exhibit strong coupling between flexural and longitudinal motion. Using a receptance-based approach, they showed that such asymmetry hybridises the wave families, creating attenuation zones and, counterintuitively, enhancing long-range transmission of longitudinal energy. Mace and Manconi [16] classified the dispersion phenomena that occur when wavemodes interact in coupled waveguides. They distinguished two weak-coupling behaviours: veering, which happens when interacting waves have group velocities of the same sign (codirectional coupling), and locking, which occurs when the group velocities are of opposite sign (contradirectional coupling). In the latter case, two dispersion branches merge into a complex-conjugate pair of wavenumbers, producing an attenuation region. The same authors studied in [17] the analogy with classical modal analysis (curve veering of natural frequencies) and with instability theory (flutter-type bifurcations), integrating the wavemode coupling concept into a broader physical context. Rughunanan et al. [18] extended the study in [16] to periodically coupled homogeneous waveguides, showing theoretically and experimentally the contradirectional coupling. Their combined perturbation, numerical, and experimental analyses confirmed this mechanism as a distinct and robust band gap formation mechanism, complementing Bragg scattering and locally resonant effects. Trainiti et al. [19] presented a seminal study on wave propagation in periodically wavy beams and plates using Floquet-Bloch theory. They showed that the geometric curvature couples longitudinal, flexural, and torsional modes, producing broad stop bands whose location and width depend on the undulation amplitude and wavelength, thus establishing undulation as a purely geometric mechanism for band gap formation and dispersion tailoring. Shi et al. [20] further demonstrated numerically and experimentally that wavy plates can support waves interactions leading to absolute band gaps by simultaneously locking different wave families. Coiling, like undulation, has also been shown to produce wide band gaps through geometric effects. In [21], theoretical and experimental studies on elastic springs with periodically discontinuous curvature were carried out, demonstrating the emergence of stop bands in their transmission characteristics. Willey et al. [22] introduced a coiled phononic structure where periodic rotational locking and geometric coiling shift Bragg-type gaps into the subwavelength regime. Their results showed that geometric reconfiguration can overcome the trade-off between wide, high-frequency Bragg gaps and narrow, locally resonant ones, highlighting geometry as an effective tool for dispersion tailoring and subwavelength attenuation. More recently, Dal Poggetto et al. [23] investigated longitudinal-flexural mode conversion in periodically undulated waveguides with constant and graded profiles, clarifying the phase-matching conditions between coupled dispersion branches. The numerical and experimental results showed that geometric undulation enables efficient broadband conversion, with graded profiles further extending the bandwidth. The study in [23] provides a description of geometry-driven codirectional coupling, complementary to the present study on contradirectional coupling and complete stop-band formation, both originating from the same dispersion-level interactions but leading respectively to energy exchange between waves or complete wave attenuation. In the context of folded structures, origami-inspired designs are an effective geometry for exploiting wave mode coupling. In particular, Miura-ori structures combine lightweight efficiency, deployability, and strong geometric interactions among axial, flexural, and torsional responses. Recent research on rotated Miura-ori tubes [24] has demonstrated tunable coupling and evidence of veering and locking. At the same time, other origami-inspired lattices have demonstrated reconfigurable gaps, programmable deformation, and unique wave phenomena [25–27]. Beyond engineering contexts, folded plate morphologies are also observed in nature, such as the corrugated shells of molluscs and the venation-guided folding of leaves, inspiring designs that utilise similar geometrical features [28]. Recent studies have also demonstrated the potential of architected metamaterials to provide simultaneous vibration isolation and multifunctional performance, particularly through the integration of nonlinear mechanisms and energy-harvesting elements. For instance, sinusoidal and hierarchical rotating–bending metamaterials have been shown to achieve low-frequency vibration isolation through quasi-zero-stiffness behaviour while simultaneously enabling electricity generation via localised deformation modes [29,30]. Although these approaches rely on nonlinear mechanisms and the integration of multifunctional materials, they highlight the broader potential of geometry-driven designs for vibration mitigation.

These developments motivate the current study, where periodic folding is investigated parametrically as a minimal geometric mechanism to induce contradirectional coupling and generate complete, subwavelength band gaps. Folded beams and plate strips are amongst the simplest geometric configurations to promote wave coupling for band gap engineering. Moreover, folded plates and beams are widely used in aerospace, civil engineering, and mechanical applications due to their high strength-to-weight ratio,

geometric efficiency, and aesthetic appeal. Compared to other architected geometries, folded beams and plates are particularly easy to be fabricated from sheet stock using established sheet-forming techniques such as press-brake bending, coining, stamping, or roll forming. These mature and scalable methods, also compatible with standard structural alloys, enable both rapid prototyping and cost efficient mass production [31].

In the present study, we first analyse the straight (planar) structure to define the reference dispersion curves, which assist in identifying *critical points*, where contradirectional band gaps may form, thereby enabling the prediction of the starting region of complete band gap formation. In continuous waveguides, contradirectional coupling typically occurs in the evanescent region of the dispersion diagram. However, when periodicity is introduced, the dispersion branches reverse slope at $\mu = \pi$, allowing them to intersect (critical points) within the propagating region. Longitudinal, flexural, and torsional Bloch waves are natural candidates for coupling under these conditions. Introducing a small folding angle activates their interactions at the critical points, giving rise to contradirectional coupling and the formation of complete band gaps. The position and width of these gaps can be tuned through geometric and material parameters, while increasing the folding angle strengthens coupling and widens the gap. This analysis identifies the conditions for mode locking, providing a means to tune the band gap frequency range before introducing further structural complexity.

Using exact DSM, [32–34], and 3D WFE models, [35–37], we separate the contribution of folding-induced coupling from Bragg scattering effects and quantify how modelling prescriptions affect the predicted band gap locations, the dominant coupling wavemode pair, and the maximum bandwidth. The comparison between beam, shell, and 3D solid models also highlights situations where simplified assumptions can fail in predicting the formation of band gaps with accuracy. The analysis distinguishes between weak coupling, where wavemode interactions are limited to localised phenomena, and strong contradirectional coupling, which reshapes the dispersion topology and produces wide complete gaps through wavemode locking. In addition to the main geometric parameters, two further geometric features that can influence coupling strength and band gap formation are studied: thickness-induced offset, which arises from the finite thickness of the waveguide and causes a lateral shift between adjoining facets when folded, [38], and fold curvature, corresponding to a finite radius along the crease lines [39]. Fold curvature, whether unintentionally introduced by manufacturing processes, such as in metallic folded plates, e.g., [31], or deliberately designed (e.g., as in corrugated or wavy structures, [23]), can enhance multi-mode coupling by promoting continuous geometric transitions between facets and folds. Thickness-induced offsets alter the relative phase between adjacent waveguides and shift band gap edges, especially when comparing idealised zero-thickness crease models with 3D models. A further effect is related to the first coupling wavemode pair, which may change depending on whether finite thickness and curvature are modelled. Such changes alter the band gap edges and determine which wave family is suppressed first, enabling different modes to be selectively targeted.

Compared with previous investigations of band gap formation in periodic structures, the present work demonstrates that folding alone acts as a minimal geometric trigger for contradirectional Bloch-wave coupling, governing the onset of dispersion-branch locking, complete band gap opening, and selective wave attenuation. Specifically, complete band gaps are shown to originate at intersections (critical points) in the unfolded dispersion topology, where enforced periodicity induces branch crossings, and folding subsequently activates wave coupling by breaking geometric symmetry and reorienting the associated wave fields. Beyond identifying the band gap mechanism, the study provides a wave-physics interpretation based on the analysis of wave polarisation through directional energy contributions, together with the evolution of wavemodes in terms of displacement fields and energy (group) velocity. This combined analysis explicitly reveals the contradirectional nature of the interacting waves responsible for complete band gap formation. By extending the investigation from beam models to fully three-dimensional formulations, the work further uncovers a hierarchy of axial-bending-torsional motion coupling, clarifying how folding geometry, thickness-induced offsets, and modelling assumptions govern the sequence of motion suppression and the resulting band gap. These findings suggest that parametric folding may serve as a geometry-driven approach to inducing complete band gaps and enabling targeted vibration attenuation, while providing insight into the use of simplified models for band gap prediction.

The rest of the paper is organised as follows. Section 2 is devoted to analysing the mechanism of complete band gap formation in periodic folded waveguides. Section 3 investigates the effects of finite thickness and fold curvature on the wave coupling strength and band gap tuning. Section 4 provides experimental validation of numerical prediction of the complete band gap. Finally, Section 5 summarises the findings.

2. Mechanism of formation of a complete band gap in a periodic folded waveguides

To study the mechanism of formation of complete band gaps induced by periodic folding in beam and plates, we use the Dynamic Stiffness Matrix (DSM) method combined with Floquet-Bloch theory and the Wave Finite Element method in its 1D formulation [35].

In real structures, fold formation typically evolves from zero to finite curvature through multiple stages, often involving localised deformation and elasto-plastic effects [40]. Moreover, at sufficiently large amplitudes or in the presence of significant pre-stress, the dispersion branches - and thus the associated coupling points and band gap edges - may become amplitude- or stress-dependent. In the present analysis, geometric and material nonlinearities are not considered, as the primary objective is to isolate and characterise the geometry-induced contradirectional coupling mechanism. Therefore, linear elastic and geometric behaviour is assumed, and small-amplitude free wave propagation is studied about the folded reference configuration. Future work could extend the study by incorporating plate-crease-plate formulations to more accurately represent local fold mechanics and their influence on wave coupling and band gap formation.

In the first part of this section, an Euler-Bernoulli beam including axial motion is analysed. The Euler-Bernoulli beam theory is strictly valid in the long-wavelength, low-frequency, regime, as it represents the leading-order term in the asymptotic expansion of the three-dimensional elasticity solution. Since the present study focuses on the first complete band gap, the use of the Euler-Bernoulli

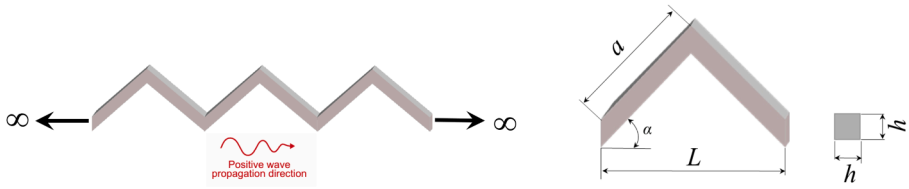

c_L [m/s]	c_T [m/s]	L [m]	h [m]
1365	815	0.022	0.001

Fig. 1. (a) Schematic representation of the periodic folded beam; (b) unit cell; (c) parameters (c_L and c_T are the phase speeds of longitudinal and torsional waves in the beam).

formulation can be assumed appropriate. However, as the cross-sectional aspect ratio increases, one-dimensional assumptions no longer capture the correct stress and displacement fields, and plate-strip or full elasticity models are required for consistent representation of the structural behaviour [41]. Accordingly, the second part of this section introduces a 3D Wave Finite Element model of a plate strip to study dispersion behaviour with multiple interacting wavemodes and their hybridisation near the coupling points.

2.1. Folded periodic beam modelled using the exact Dynamic Stiffness Matrix method (DSM)

In this section the frequency-dependent stiffness matrix $\mathbf{D}(\omega)$, based on the exact equations of motion of an Euler-Bernoulli beam in bending and axial vibration, is used to model the unit cell of a folded beam. Fig. 1 shows a schematic representation of the folded beam, along with the unit cell, the geometric parameters, and the phase velocity of longitudinal and torsional waves. Fig. 2 depicts a schematic representation of the periodic beam and the unit cells, where $u(x)$, $v(x)$ and $\theta(x)$ are axial, transverse, and rotational displacements. Internal forces are given by the axial $U(x)$ and shear $V(x)$ forces, and bending moment $M(x)$. The DSM for beam cases has been extensively discussed and illustrated in the literature, e.g., [32,33,42], and only the matrix terms, with reference to Eq. (5), are provided in Appendix A for completeness.

Following the approach presented in [16], we first consider an uncoupled system, which in our case corresponds to the straight periodic beam, Fig. 2(a). To clearly distinguish the effects of periodicity from those caused by axial-bending coupling due to folding, the model is extended by adding periodically distributed lumped masses $M = \frac{1}{10} M_{\text{unit cell}}$. This enables a straightforward examination of how band gaps form, either through Bragg effects or wave coupling. The dispersion curves of the straight beam provide the reference curves for the location of critical points, which can serve as a reference for the formation of the contradirectional band gap. As shown in Fig. 2(b), the folding is introduced in the model by the angle α. In the folded configuration, the unit cell can be seen as made by two connected beams: the left beam rotated by an angle α with respect to the global reference frame, and the right beam rotated by an angle $-\alpha$.

The equation of motion of the unit cell is given by

$$\begin{bmatrix} \mathbf{D}_{\text{LL}} & \mathbf{D}_{\text{LI}} & \mathbf{0} \\ \mathbf{D}_{\text{IL}} & \mathbf{D}_{\text{II}} & \mathbf{D}_{\text{IR}} \\ \mathbf{0} & \mathbf{D}_{\text{RI}} & \mathbf{D}_{\text{RR}} \end{bmatrix} \begin{Bmatrix} \mathbf{q}_L \\ \mathbf{q}_I \\ \mathbf{q}_R \end{Bmatrix} = \begin{Bmatrix} \mathbf{f}_L \\ \mathbf{f}_I \\ \mathbf{f}_R \end{Bmatrix}, \quad \begin{array}{l} \mathbf{q}_L = \{u(0), v(0), \theta(0)\}^T;\ \mathbf{f}_L = \{U(0), V(0), M(0)\}^T \\ \mathbf{q}_I = \{u(a), v(a), \theta(a)\}^T;\ \mathbf{f}_I = \{U(a), V(a), M(a)\}^T \\ \mathbf{q}_R = \{u(L), v(L), \theta(L)\}^T;\ \mathbf{f}_R = \{U(L), V(L), M(L)\}^T \end{array} \tag{1}$$

where $a = L\sec(\alpha)/2$. The effect of the attached masses is included in the formulation by the dynamic matrix $\mathbf{D}_0$

$$\mathbf{D}_0 = \begin{bmatrix} -\omega^2 M_0 & 0 & 0 \\ 0 & -\omega^2 M_0 & 0 \\ 0 & 0 & 0 \end{bmatrix}. \tag{2}$$

Each beam of the unit cell in Fig. 2(b) is modelled as a single spectral Euler-Bernoulli beam element of length a. In their respective local reference frames, the DSMs ($\mathbf{D}_{1loc}$ and $\mathbf{D}_{2loc}$) are obtained using the formulation reported in Appendix A. To express these

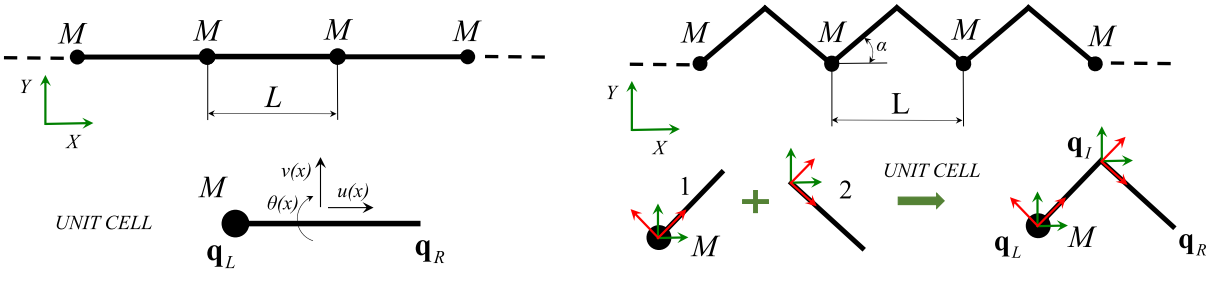

Fig. 2. Beam modelled using the exact DSM matrix with periodically attached masses M. (a) Uncoupled system: straight periodic beam; (b) coupled system: periodic beam folded by an angle α. Global and local reference systems and generalised coordinates are illustrated.

matrices in the global reference frame, they are rotated using

$$\mathbf{D}_1 = \mathbf{R}^T \mathbf{D}_{1loc} \mathbf{R}; \quad \mathbf{D}_2 = \mathbf{R} \mathbf{D}_{2loc} \mathbf{R}^T; \tag{3}$$

where $\mathbf{R}$ is the rotation matrix

$$\mathbf{R} = \begin{bmatrix} \mathbf{r} & \mathbf{0} \\ \mathbf{0} & \mathbf{r} \end{bmatrix}, \quad \mathbf{r} = \begin{bmatrix} \cos(\alpha) & -\sin(\alpha) & 0 \\ \sin(\alpha) & \cos(\alpha) & 0 \\ 0 & 0 & 1 \end{bmatrix}. \tag{4}$$

The finite rotation associated with folding is introduced through the rotation matrices in Eqs. (3)-(4), without any small-angle approximation. The resulting equations therefore capture the coupling induced by the fold geometry, while the amplitude and strains associated with wave propagation are described within linear assumptions.

The dynamic matrix $\overline{\mathbf{D}}$ of the assembled system in terms of $\mathbf{q}_L$ and $\mathbf{q}_R$ can be reformulated by dynamic condensation of the internal nodes, yielding

$$\begin{bmatrix} \overline{\mathbf{D}}_{LL} & \overline{\mathbf{D}}_{LR} \\ \overline{\mathbf{D}}_{RL} & \overline{\mathbf{D}}_{RR} \end{bmatrix} \begin{Bmatrix} \mathbf{q}_L \\ \mathbf{q}_R \end{Bmatrix} = \begin{Bmatrix} \mathbf{f}_L \\ \mathbf{f}_R \end{Bmatrix}. \tag{5}$$

Equation (5) can also be rewritten using transfer matrix $\mathbf{T}$, which relates the left and right state vectors as

$$\begin{bmatrix} \mathbf{T}_{11} & \mathbf{T}_{12} \\ \mathbf{T}_{21} & \mathbf{T}_{22} \end{bmatrix} \begin{Bmatrix} \mathbf{q}_L \\ \mathbf{f}_L \end{Bmatrix} = \begin{Bmatrix} \mathbf{q}_R \\ \mathbf{f}_R \end{Bmatrix} \tag{6}$$

where $\mathbf{T}_{11} = -\overline{\mathbf{D}}_{LR}^{-1} \overline{\mathbf{D}}_{LL}$, $\mathbf{T}_{12} = -\overline{\mathbf{D}}_{LR}^{-1}$, $\mathbf{T}_{21} = \overline{\mathbf{D}}_{RL} - \overline{\mathbf{D}}_{RR} \overline{\mathbf{D}}_{LR}^{-1} \overline{\mathbf{D}}_{LL}$, and $\mathbf{T}_{22} = -\overline{\mathbf{D}}_{RR} \overline{\mathbf{D}}_{LR}^{-1}$. From the state variables defined at the unit-cell boundaries, the Floquet theorem, together with the equilibrium of external forces, leads to the following relationship:

$$\mathbf{q}_R = \lambda \mathbf{q}_L; \quad \mathbf{f}_R = -\lambda \mathbf{f}_L, \tag{7}$$

where $\lambda = \mathrm{e}^{-\mathrm{i}\mu}$, $\mathrm{i} = \sqrt{-1}$ is the imaginary unit, and μ is the propagation constant. Wave types occur in pairs, each consisting of positive- and negative-going components, characterised by complex propagation constants, $\mu = \mathrm{Re}(\mu) \pm \mathrm{i}\ \mathrm{Im}(\mu)$, where the real part $\mathrm{Re}(\mu)$ represents the phase constant, and the imaginary part $\mathrm{Im}(\mu)$ denotes the attenuation constant. In the following, lossless waveguides are considered; therefore, purely real values of μ correspond to propagating waves, purely imaginary values to evanescent waves, and complex values to attenuating waves. The free-wave propagation problem is here solved by prescribing the (real) frequency ω and computing the (complex) propagation constant μ. This approach conveniently provides direct information on the attenuation behaviour within the band gaps. Frequency bands in which $\mathrm{Im}(\mu) \neq 0$ are the band gaps, also referred as attenuation zones, since no net transport of vibrational energy occurs and the wave amplitude decays progressively along unit cells.

The values of λ are obtained by solving one of the following eigenvalue problems:

$$\det\left(\mathbf{T} - \lambda \mathbf{I}\right) = 0, \quad \text{or} \quad \det\left([\mathbf{I}\ \lambda^{-1}\mathbf{I}]\, \overline{\mathbf{D}}\, [\mathbf{I}\ \lambda \mathbf{I}]^T\right) = 0. \tag{8}$$

Since $\mathbf{T}$ is a real 6x6 symplectic matrix, the first of Eqs. (8) can be rewritten as

$$\lambda^6 + I_1 \lambda^5 + I_2 \lambda^4 + I_3 \lambda^3 + I_2 \lambda^2 + I_1 \lambda + 1 = 0, \tag{9}$$

where the real coefficients I_1, I_2 and I_3 are the first three invariants of the transfer matrix $\mathbf{T}$. These can be obtained by means of the Faddeev-LeVerrier algorithm, presented below in its generalised recursive formulation

$$I_0 = 1, \quad I_k = -\frac{1}{k} \sum_{i=1}^{k} I_{k-i}\ \mathrm{tr}(\mathbf{T}^i) \quad \text{for} \quad k = 1, \ldots, n. \tag{10}$$

Figure 3 shows the dispersion curves of the periodic straight beam (uncoupled system) and of the corresponding beam folded by a small angle $\alpha = 1^o$ (coupled system). Only propagation constants with positive real part and negative imaginary part, $\mathrm{Re}(\mu) > 0$ and $\mathrm{Im}(\mu) < 0$, are presented using the non-dimensional frequency

$$\Omega_b = \frac{\omega}{\omega_{b,1}}, \quad \omega_{b,1} = \left(\frac{n\pi}{L}\right)^2 \sqrt{\frac{D}{\rho A}}; \quad n = 1, \tag{11}$$

where $D = EI$ is the bending stiffness of the beam and A is the cross-sectional area of the beam. In Eq. (11), $\omega_{b,1}$ is the lowest Bragg frequency of the flexural waves, which also corresponds to the lowest natural frequency of the simply supported straight beam of length L in bending $k_b L = \pi$, where k_b, defined in Appendix A, denotes the flexural wavenumber [43].

The dispersion curves in Fig. 3 describe the relationship between the frequency and the complex wavenumber μ for all possible wavemodes supported by the structure. Complex values of μ, corresponding to attenuating waves, occur in conjugate pairs whose superposition results in zero net energy transport. The shift from purely real to complex or purely imaginary values of μ marks the boundary between propagation and attenuation zones. Bragg band gaps are highlighted in yellow in the figure; the upper edges of these band gaps correspond to $\omega_{b,1}$ and $\omega_{b,2}$. Two wavemodes can be identified: branch 1, characterised by axial deformation along the beam axis, and branch 2, characterised by motion in the perpendicular direction to the direction of wave propagation. At low frequency, these correspond to longitudinal and flexural waves.

Figure 3(a) shows that the longitudinal (1) flexural (2) branches cross at the critical points P and Z. Fig. 3(b) shows dispersion curves when a small folding angle (weak coupling) is introduced. This modifies the dispersion characteristics near the critical points

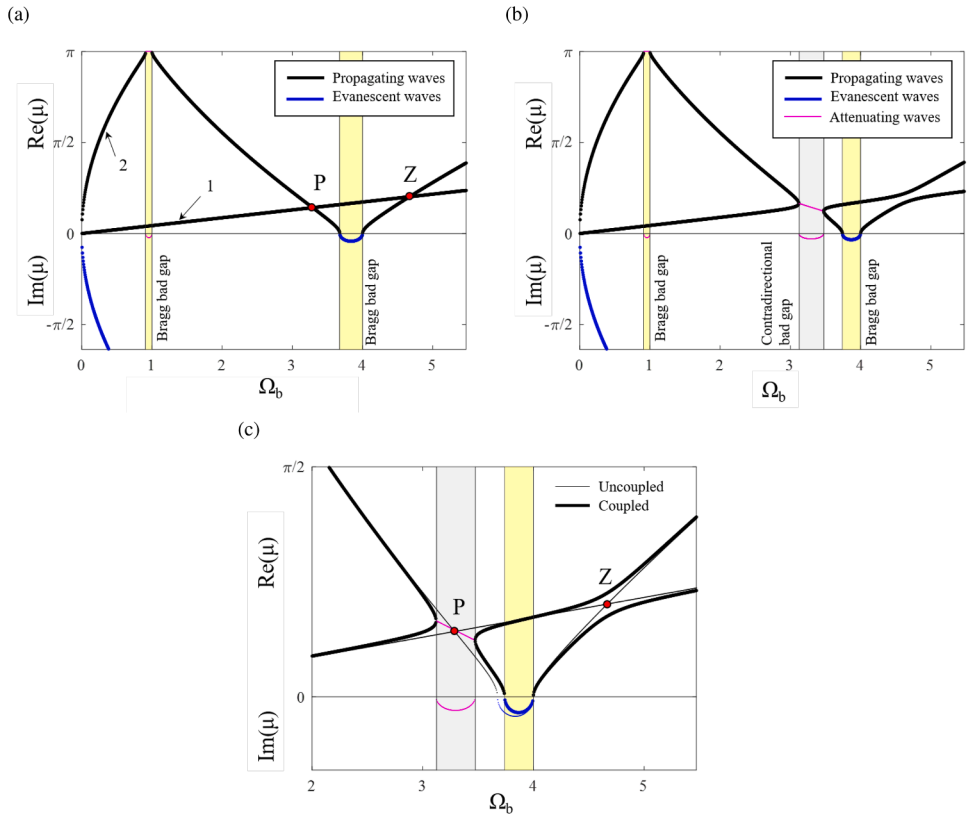

Fig. 3. Periodic beam modelled using the exact DSM matrix. Complex dispersion curves for wave propagation in the positive x direction: (a) uncoupled system: straight periodic beam $\alpha = 0^o$; (b) coupled system: folded beam, $\alpha = 1^o$; (c) dispersion curves near the critical points: Z veering (codirectional coupling); P locking (contradirectional coupling, complete gap); thin lines represent the backbone curves corresponding to the uncoupled system in (a). Black lines: pure propagating waves; blue lines: evanescent waves; magenta thin lines: complex-conjugate propagation constant (only the branches with positive real and negative imaginary part are shown). Grey region: contradirectional coupling-induced complete band gap; yellow region: Bragg-type band gaps. (For interpretation of the references to colour in this figure, the reader is referred to the web version of this article.)

and two phenomena occur: veering, near point Z, where branch 1 and branch 2 approach with slope of the same sign (same direction of the energy velocity) and repel each other; locking, near point P, where branch 1 and branch 2 approach with slope of opposite sign (opposite directions of energy velocity) and they lock, forming a new complete contradirectional band gap highlighted in grey in the figure. The phenomena are better illustrated in Fig. 3(c), where thin lines represent the dispersion curves of the uncoupled system.

2.1.1. Parametric analysis

The vibration attenuation capability of the proposed structure can be studied by examining how the dispersion curves change with the angle α. The effect of parameter variation on the formation of a complete band gap can be visualised using both the attenuation-constant-surfaces, as in [44], and the band-edge-surfaces that separate complex propagation domains [45]. The attenuation-constant-surfaces quantify attenuation within complete stop bands by plotting the minimum imaginary part of μ versus the parameter α. This value can serve as an indicator of the wave and vibration attenuation performance. The band-edge-surfaces are obtained from Eq. (9), expressed in terms of the propagation constant μ:

$$(e^{-3i\mu} + e^{3i\mu}) + I_1(e^{-2i\mu} + e^{2i\mu}) + I_2(e^{-i\mu} + e^{i\mu}) + I_3 = 0. \tag{12}$$

After some algebraic manipulations, it is possible to express the characteristic polynomial as a cubic equation in $\cosh(i\mu)$:

$$\cosh^3(i\mu) + \frac{1}{2}I_1\cosh^2(i\mu) + \frac{1}{4}(I_2 - 3)\cosh(i\mu) + \frac{1}{8}(I_3 - 2I_1) = 0. \tag{13}$$

The wave propagation characteristics of the periodic structure can be visually represented in the space of the invariants (I_1, I_2, I_3). By examining the roots of Eq. (13) with respect to $\cosh(i\mu)$, four distinct surfaces, labelled as R, S, and $P_{1,2}$, partition the invariant space into regions corresponding to different propagation behaviours. The curves R and S are obtained when $\cosh(i\mu) = \pm 1$:

$$R := \{(I_1, I_2, I_3) \mid 2 - 2I_1 + 2I_2 - I_3 = 0\}, \tag{14}$$

$$S := \{(I_1, I_2, I_3) \mid 2 + 2I_1 + 2I_2 + I_3 = 0\}, \tag{15}$$

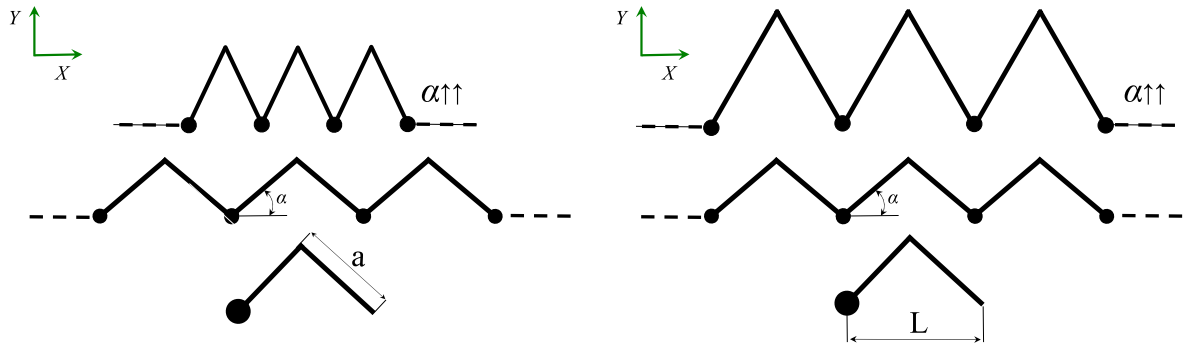

Fig. 4. Schematics illustration of the two parametric analyses with respect to α: (a) constant fold length a (b) constant periodic length L.

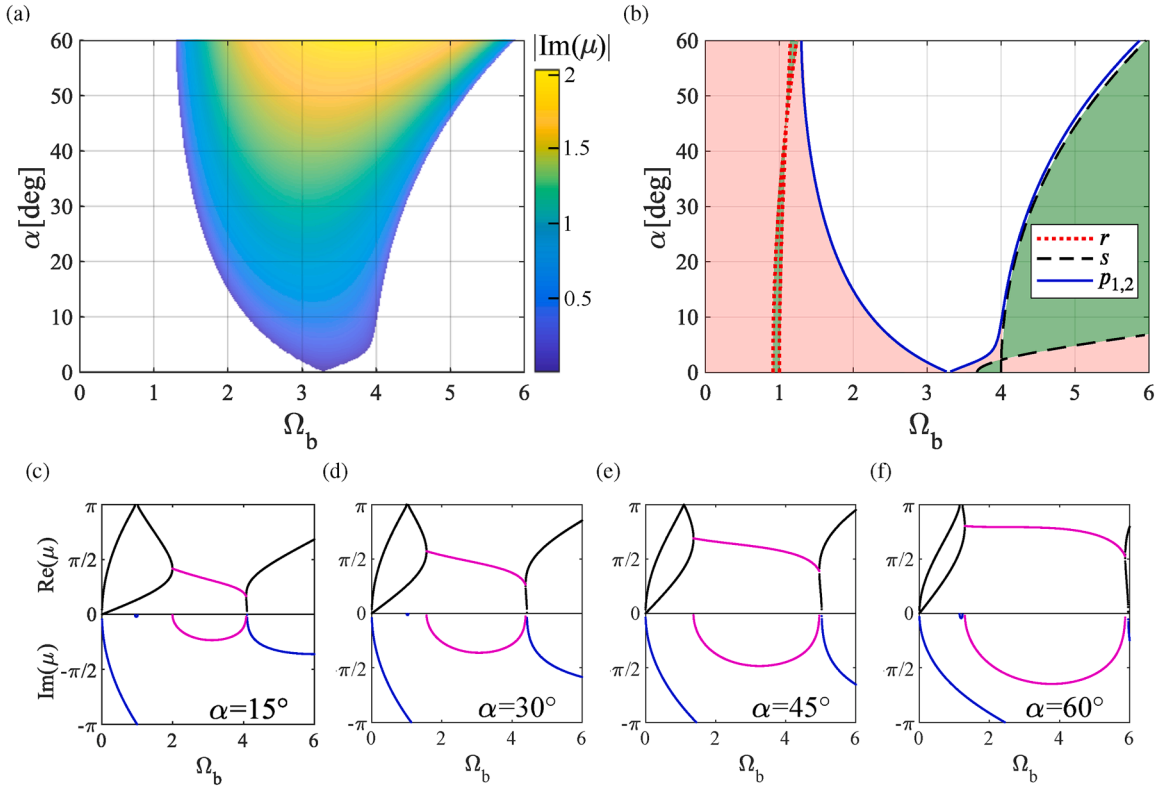

Fig. 5. Effects of the folding angle α when the fold length a is constant: (a) planform view of the attenuation-constant-surface (the lateral bar shows the attenuation level, $\min|\mathrm{Im}(\mu)|$). (b) Projection of the R, S and $P_{1,2}$ surfaces on the $\alpha-\Omega_b$ plane: the regions highlighted in red correspond to cases where two branches in the dispersion diagram are real and one branch is imaginary (two propagating waves and one evanescent wave); the regions highlighted in green correspond to cases where two branches are imaginary and one is real (one propagating waves and two evanescent wave); the unshaded regions correspond to the complete band gaps. (c) Dispersion curves for $\alpha = 15°$. (d) Dispersion curves for $\alpha = 30°$. (e) Dispersion curves for $\alpha = 45°$. (f) Dispersion curves for $\alpha = 60°$. (For interpretation of the references to colour in this figure, the reader is referred to the web version of this article.)

while $P_{1,2}$ surfaces divide complex roots from real roots:

$$P_{1,2} := \{(I_1, I_2, I_3) \mid 27I_1 - 27I_3 - 2I_2^3 \pm 2\sqrt{(9 + I_1^2 - 3I_2^2)} \tag{16}$$

In the proposed bivariate parametric analysis in Ω_b and α, the band-edge curves (denoted as r, s, and $p_{1,2}$, respectively) are determined by projecting the loci of the R, S, and $P_{1,2}$ surfaces onto the corresponding α-Ω_b plane.

Two parametric analyses with respect to α are presented, as illustrated in Fig. 4. In the first case, Fig. 4(a), the periodic length L along the x-axis is prescribed while the length of the folds a varies as $L/2\sec(\alpha)$. In the second case, Fig. 4(b), the length a of the folds is prescribed, and the period L varies with $2a\cos(\alpha)$. The comparison between these two cases emphasises the different effects of the folding parameters on band gap formation and attenuation characteristics of the structure.

Figures 5 and 6 show the maps of the complete band gaps as a planform view of the attenuation-constant-surfaces, Figs. 5(a) and 6(a), and the evolution of the band structure and band-edge curves (r, s, and $p_{1,2}$), Figs. 5(b) and 6(b). Dispersion curves for $\alpha = 15°$, 30°, 45°, and 60° are also shown Figs. 5(c-f) and 6(c-f). The maps of the pass and band regions identify three distinct regions: the red region, characterised by one propagating wave and two evanescent waves (two purely imaginary and one purely real propagation constants in the dispersion diagram); the green region, characterised by two propagating waves and one evanescent wave (two purely real and one purely imaginary propagation constants in the dispersion diagram); the unshaded white regions, corresponding to the complete band gaps (areas where all the propagation constants are either complex or purely imaginary).

When the fold length a is kept constant as α varies, (Fig. 5), a single complete band gap is formed as a result of contradirectional coupling induced by the folding angle. The band gap width increases with α, while $Im(\mu)$ rises accordingly, indicating stronger wave attenuation. The case with a constant periodic length L, Fig. 6, exhibits a more complex behaviour. The complete band gap associated with the contradirectional coupling increases in bandwidth up to a maximum at approximately 26°, and then decreases. The attenuation constant μ, on the other hand, increases with increasing α. In addition to this primary complete band gap, three further complete band gaps, characterised by purely imaginary propagation constants, are observed. These additional stop bands, located in the upper-right region of Fig. 6(b), are bounded by the r (red dashed lines), s (black dashed lines) curves. The formation of the higher-frequency band gaps mainly results from changes in the total mass and geometry of the unit cell rather than from a contradirectional coupling mechanism: maintaining a fixed lattice constant L while varying α, in fact, implies an increase in the fold length a, which then raises the unit-cell mass and alters its internal topology. This variation leads to a progressive downward shift of the higher-order Bragg-type band gaps.

The results show that the formation of complete band gaps in the folded plate structure provides an intrinsic mechanism for broadband vibration isolation. Within the band gap frequency range, wave propagation is attenuated in all directions, resulting in a strong reduction in vibration transmission without relying on local resonators, active control, or nonlinear stiffness effects. Compared with other mechanisms for vibration isolation, folding exploits only geometry-induced wave coupling in the linear regime, offering a predictable and directionally invariant attenuation mechanism.

2.2. Folded periodic plate strip modelled using a 3D Wave Finite Element method

A schematic representation of the folded plate strip and its corresponding WFE unit-cell model is shown in Fig. 7. The same material and geometric parameters used in Section 2.1 are assumed. The Wave Finite Element method is applied, and the dynamic stiffness matrix of the unit cell is calculated as $\mathbf{D}(\omega) = \mathbf{K} - \omega^2\mathbf{M}$, where the mass $\mathbf{M}$ and stiffness $\mathbf{K}$ matrices are obtained from a standard FE analysis. The unit cell is discretised using 200 eight-node solid elements, each having three translational degrees of freedom per node (displacements in the X, Y, Z directions).

The uncoupled system is defined as a plane plate strip. Compared to the beam case, no additional masses are included, but dispersion curves are still calculated assuming structural periodicity L, resulting in a change in the slope of the branches when $\mu = \pi$. The coupled system corresponds to the plate strip periodically folded by an angle α.

Figure 8 illustrates the complex dispersion curves for both the plane and the folded plate strip. Results are presented using the nondimensional frequency

$$\Omega_p = \frac{\omega}{\omega_{p,1}}, \quad \omega_{p,1} = \left(\frac{\pi}{L}\right)^2 \sqrt{\frac{D}{\rho h}}; \tag{17}$$

where $D = Eh^3/(12(1-\nu))$ is the bending stiffness of the plate. Four types of dispersion branches can be identified within the considered frequency range: longitudinal (branch 1), out-of-plane flexural (branch 2), in-plane flexural (branch 3), torsional (branch 4). The longitudinal waves exhibit non-dispersive behaviour, the flexural are strongly dispersive, with phase velocity increasing with frequency, while the torsional waves are weakly dispersive. As the frequency increases, additional branches can cut-off corresponding to higher-order wavemodes. In addition, the introduction of folding gives rise to a higher-order branch that cut-off at $\Omega_p = 4.51$. The longitudinal (branch 1) and flexural (branch 2) wavemodes exhibit the same characteristics to those observed in the beam case, intersecting at points P and Z. The torsional and in-plane flexural modes intersect at point Q. The order at which these critical points appear in the dispersion diagram depends on the plate geometry. As an example, point Q - where the torsional (branch 4) and in-plane flexural (branch 3) wavemodes intersect - can be tuned by varying the plate width b. When a small folding angle of $\alpha = 1°$ is introduced, weak coupling arises and a contradirectional coupling band gaps form when two interacting branches exhibit opposite slopes, corresponding to opposite group velocities, as shown in Fig. 8(b). This coupling occurs between branch 1 and branch 2 (longitudinal and out-of-plane flexural modes), and between branch 3 and branch 4 (in-plane flexural and torsional modes). The coupling mechanisms are illustrated in detail near the critical interaction points in Fig. 8(c), where the thin black lines denote the reference dispersion curves of the corresponding uncoupled (plane plate) system.

Figure 9 shows the dispersion curves when $\alpha = 45°$. The shaded grey region denotes the complete band gap, which results from strong contradirectional coupling between the interacting wavemodes. To show the nature of the different propagating and attenuating modes, the corresponding displacement fields of the waves labelled A-U are illustrated in Figs. 9-10. Animations of the plate-strip motion associated with these waves are provided as supplementary material. The deformations shown in the wavemode plots and animations are not to scale and have been amplified to highlight the structure's motion under the passage of the wave.

The nature of the wavemodes in Figs. 9–10, and their behaviour near the coupling points P, Q, and the uncoupling point N, is examined using the time-averaged energy density, $\langle E \rangle$, under the passage of the wave (μ_j, ω_j), which is calculated by summing the

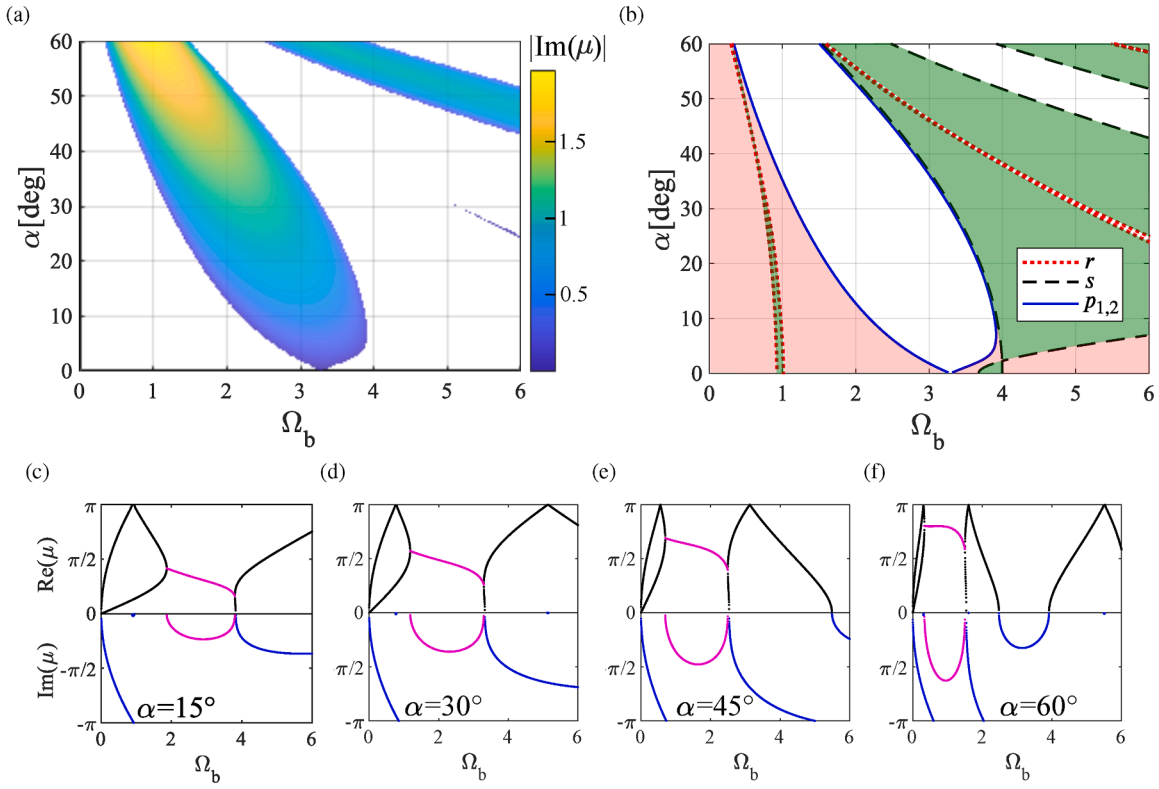

Fig. 6. Parametric analysis. Effects of the folding angle α when the periodic length L is constant: (a) planform view of the attenuation-constant-surface (the lateral bar shows the attenuation level, $\min|\mathrm{Im}(\mu)|$). (b) Projection of the R, S and $P_{1,2}$ surfaces on the $\alpha - \Omega_b$ plane: the regions highlighted in red correspond to cases where two branches in the dispersion diagram are real and one branch is imaginary (two propagating waves and one evanescent wave); the regions highlighted in green correspond to cases where two branches are imaginary and one is real (one propagating waves and two evanescent wave); the unshaded regions correspond to the complete band gaps. (c) Dispersion curves for $\alpha = 15°$. (d) Dispersion curves for $\alpha = 30°$. (e) Dispersion curves for $\alpha = 45°$. (f) Dispersion curves for $\alpha = 60°$. (For interpretation of the references to colour in this figure, the reader is referred to the web version of this article.)

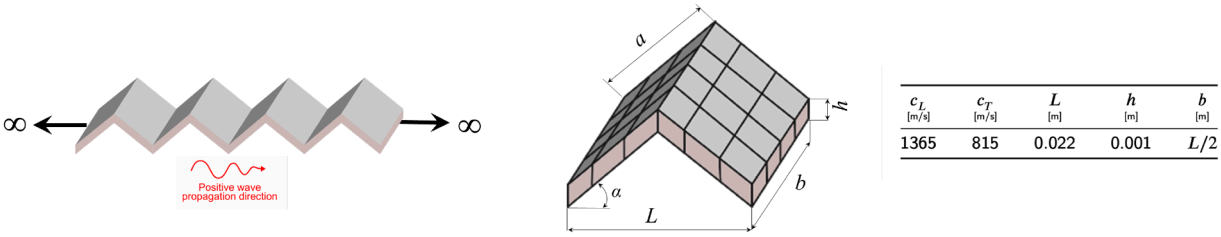

c_L [m/s]	c_T [m/s]	L [m]	h [m]	b [m]
1365	815	0.022	0.001	$L/2$

Fig. 7. (a) Schematic representation of the folded periodic plate; (b) WFE unit cell; (c) parameters.

time-averaged kinetic energy $\langle E_k \rangle$ and the time-averaged potential energy $\langle E_p \rangle$ stored in the unit cell:

$$\langle E \rangle_j = \langle E_k \rangle_j + \langle E_p \rangle_j = \frac{\omega^2}{4} \mathrm{Re}\left[\mathbf{q}_j^* \mathbf{M} \mathbf{q}_j\right] + \frac{1}{4} \mathrm{Re}\left[\mathbf{q}_j^* \mathbf{K} \mathbf{q}_j\right] \tag{18}$$

where $\mathbf{q}_j$ are the displacements of the nodes of the unit cell. An effective way to characterise the nature of the wavemodes is evaluating the distribution of kinetic energy among the X, Y, and Z directions. The corresponding percentages are reported in Tables 1 and 2. Another useful energy-related quantity is the energy velocity, obtained here as the ratio between the time-averaged energy flow and the time-averaged stored energy density within one unit cell

$$v_{ej} = \frac{\frac{\omega}{2} \mathrm{Im}\left(\mathbf{F}_{Lj}^* \mathbf{q}_{Lj}\right)}{\langle E \rangle_j / L}. \tag{19}$$

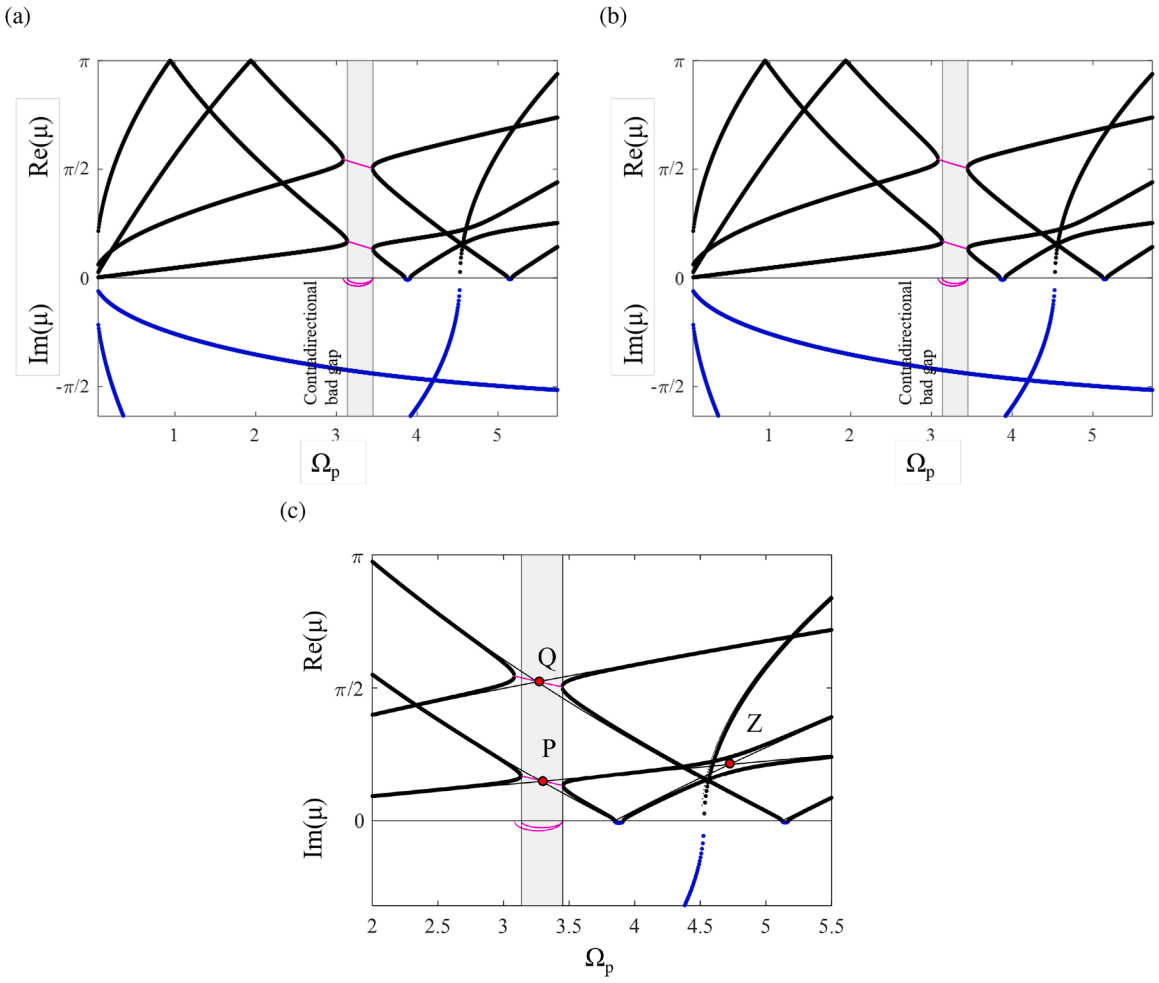

Fig. 8. Periodic plate strip modelled using the WFE method. Complex dispersion curves for wave propagation in the positive x direction: (a) uncoupled system: plane periodic plate $\alpha = 0^o$; (b) coupled system: periodically folded plate, $\alpha = 1$; (c) dispersion curves near the critical points: Z veering (codirectional); P and Q locking (contradirectional, complete gap); thin lines represent the backbone curves corresponding to the uncoupled system in (a). Black lines: pure propagating waves; blue lines: evanescent waves; magenta thin lines: complex-conjugate propagation constant (only the branches with positve real and negative imaginary parts are shown). Grey region: contradirectional coupling-induced complete band gap. (For interpretation of the references to colour in this figure, the reader is referred to the web version of this article.)

Table 1
Energy velocity and directional distribution of the time-averaged kinetic energy in the X, Y, and Z directions for the wavemodes labelled A-D in Fig. 9.

Label	Ω	μ	E_x/E_{tot} (%)	E_y/E_{tot} (%)	E_z/E_{tot} (%)	v_e (m/s)
A	0.3587	0.96	1.13	79.47	19.4	0.0121
B	0.2662	0.80	96.05	0	3.95	0.0018
C	0.2903	1.92	4.33	94.51	1.16	0.0081
D	0.2782	2.51	34.19	0	65.81	0.0026

For lossless waveguides, the energy velocity coincides with the group velocity, corresponding to the slope of the branches in the dispersion diagram.

From the reconstructed displacement fields and the kinetic energy distributions reported in Fig. 9 and Table 1, it can be seen that the wavemodes become hybridised due to folding: wave A corresponds to a quasi-torsional mode, with approximately 80% of the motion in the Y direction and 20% in the out-of-plane Z direction; wave B exhibits a quasi-longitudinal behaviour, dominated by motion in the propagation direction X (about 96%), with a small out-of-plane contribution (approximately 4%); wave C represents

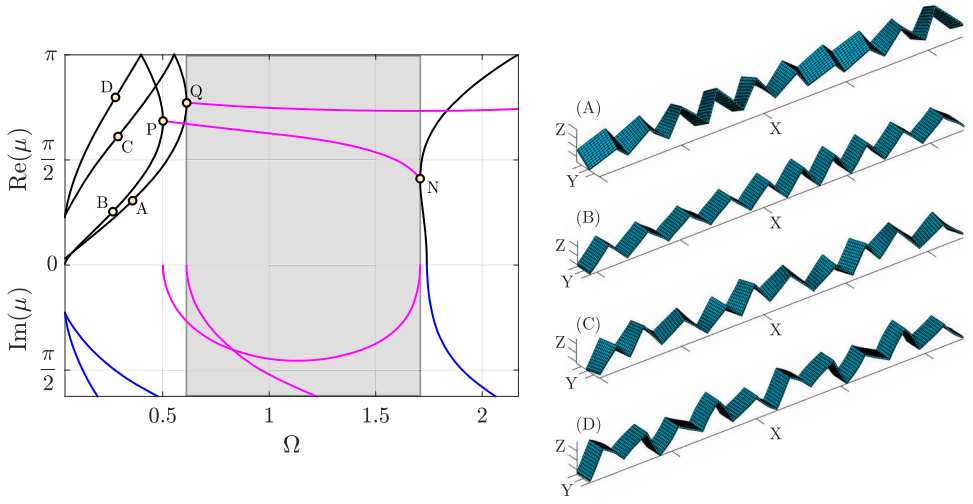

Fig. 9. Periodic folded plate strip modelled using the WFE method for $\alpha = 45°$. Complex dispersion curves and corresponding wavemodes for propagation in the positive x-direction. Black lines denote pure propagating waves; blue lines represent evanescent waves; and thin magenta dotted lines indicate complex-conjugate solutions within the contradirectional band gap (only branches with positve real and negative imaginary parts are shown). The displacement fields associated with the individual wavemodes labelled A-D are also illustrated (not to scale). Animations of the plate-strip motion associated with these waves are provided as supplementary material. (For interpretation of the references to colour in this figure, the reader is referred to the web version of this article.)

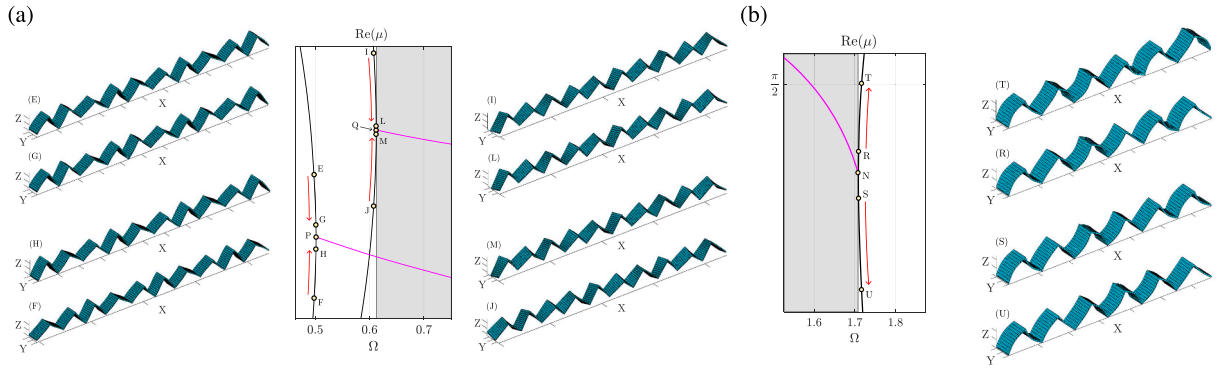

Fig. 10. Periodic folded plate strip modelled using the WFE method when $\alpha = 45^o$: a) wave behaviour near the coupling points P and Q; b) complex dispersion curves and wavemodes in the vicinity of the unlocking point N. Displacement fields corresponding to the individual wavemodes are shown (not to scale). Animations of the plate-strip motion associated with these waves are provided as supplementary material.

Table 2
Energy velocity and directional distribution of the time-averaged kinetic energy in the X, Y, and Z directions for the wavemodes labelled E-U in Fig. 10.

Label	Ω	μ	E_x/E_{tot} (%)	E_y/E_{tot} (%)	E_z/E_{tot} (%)	$v_e \times 10^4$ (m/s)
E	0.4980	2.31	69.9	0	30.1	-9.27
F	0.4980	2.00	78.8	0	23.2	9.03
G	0.5012	2.19	72.8	0	27.2	-1.83
H	0.5012	2.13	74.1	0	25.9	1.82
I	0.6074	2.62	5.4	85.4	9.2	-48.48
J	0.6074	2.23	4.5	83.6	11.9	48.80
L	0.6119	2.44	5.0	84.5	10.5	≃0
M	0.6119	2.42	5.0	84.5	10.5	≃0
R	1.7092	1.36	88.6	0	11.4	213.34
S	1.7092	1.20	90.9	0	9.1	-149.24
T	1.7164	1.58	84.9	0	15.1	1688.69
U	1.7164	0.91	94.8	0	5.2	-345.42

a quasi-flexural in-plane mode, with nearly 95% of the motion in the Y direction and about 4% in the X direction, whereas wave D corresponds to a quasi-flexural out-of-plane mode, with about 65% of the motion in the Z direction and 35% in the X direction.

Figure 10, together with Table 2, illustrates the evolution of the wavemodes in the vicinity of the coupling points P, Q, and uncoupling point N. At point P, the quasi-flexural and quasi-longitudinal wave pair (E and F) propagate in opposite directions, as indicated by their slope and the energy velocities reported in Table 2. With increasing frequency, these modes gradually transform into waves G and H, which display nearly identical kinetic energy distributions (approximately 75% in the X direction and 25% in the Z direction) and equal but opposite energy velocities. At the coupling point P, the two wavemodes show identical characteristics and energy velocities and coalesce, giving rise to a pair of complex-conjugate waves with zero net energy transport. This behaviour is characteristic of the locking mechanism associated with contradirectionally coupled waves. The same is observed at point Q, where the torsional and in-plane flexural wavemodes form a coupled pair. These modes also interact in a contradirectional manner, producing complex-conjugate solutions with vanishing energy velocity. Hence, points P and Q represent two distinct instances of locking in the folded plate: the first involving longitudinal/out-of-plane flexural coupling, and the second torsional/in-plane flexural coupling. Together, these interactions give rise to the formation of a complete band gap. At point N, the quasi-longitudinal and quasi-flexural branches, previously locked as a pair of non-propagating complex-conjugate waves, unlock into two new propagating wavemodes travelling in opposite directions. These new wavemodes, labelled R and S, progressively diverge and recover their predominant characteristics, while transporting energy in opposite directions (waves T and U). This transition marks the reopening of the propagating branches, where two attenuating solutions revert to a pair of real modes with opposite group velocities. A similar unlocking mechanism is observed at higher frequencies for the same family of coupled branches.

3. Influence of thickness and crease curvature modelling on the complete band gap

In this section, the influence of modelling assumptions related to finite thickness and crease curvature on the predicted position and width of the first complete band gaps in folded plates is investigated. These aspects are often neglected in idealised models of folded structures, where the geometric eccentricity associated with finite thickness is not modelled and adjacent panels are assumed to meet along a common fold line with a sharp crease. The same reasoning is used for the crease of the folds, because manufacturing

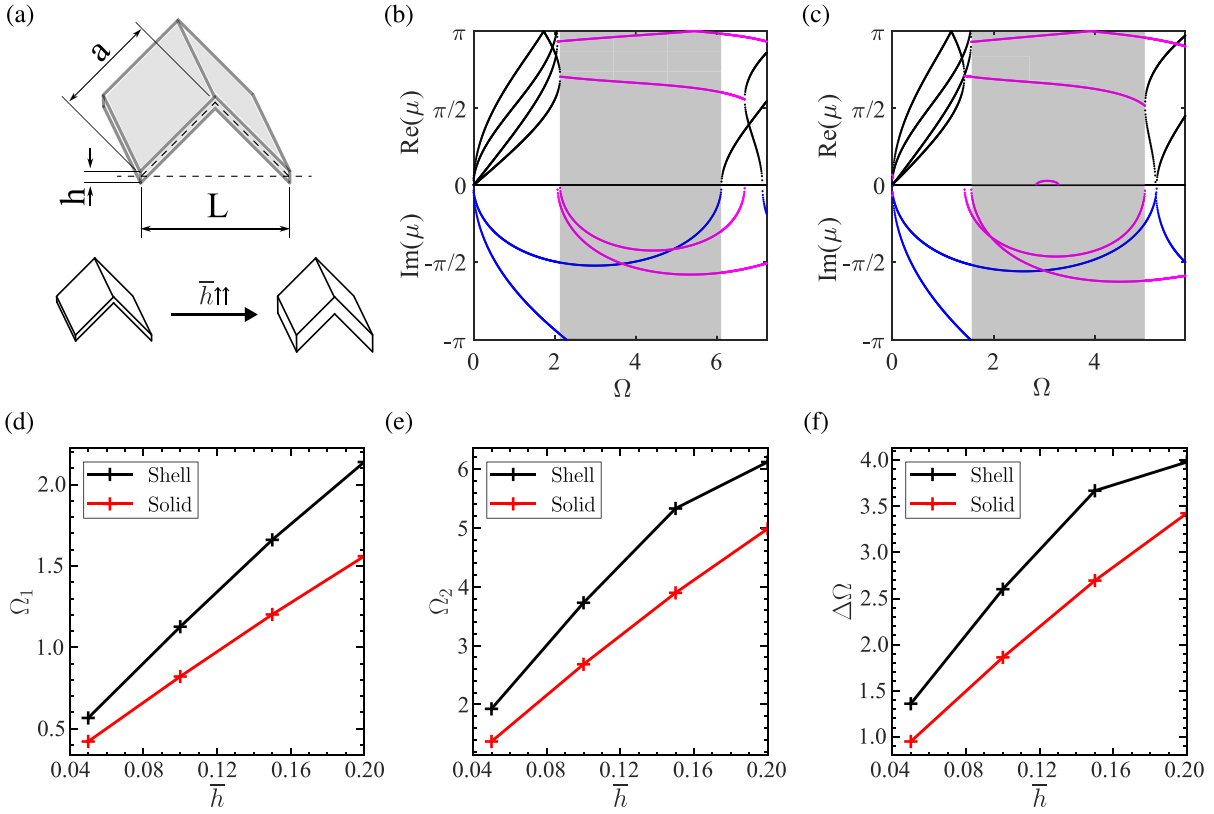

Fig. 11. Effect of nondimensional thickness $\overline{h}$: (a) schematic figure of the unit cell; (b) dispersion curves from the shell model (zero thickness) for $\overline{h} = 0.2$; (c) dispersion curves from the 3D solid WFE model (finite thickness) for $\overline{h} = 0.2$; (d-f) evolution of the lower and upper band gap edges and the corresponding bandwidth of the first complete band gap with increasing $\overline{h}$.

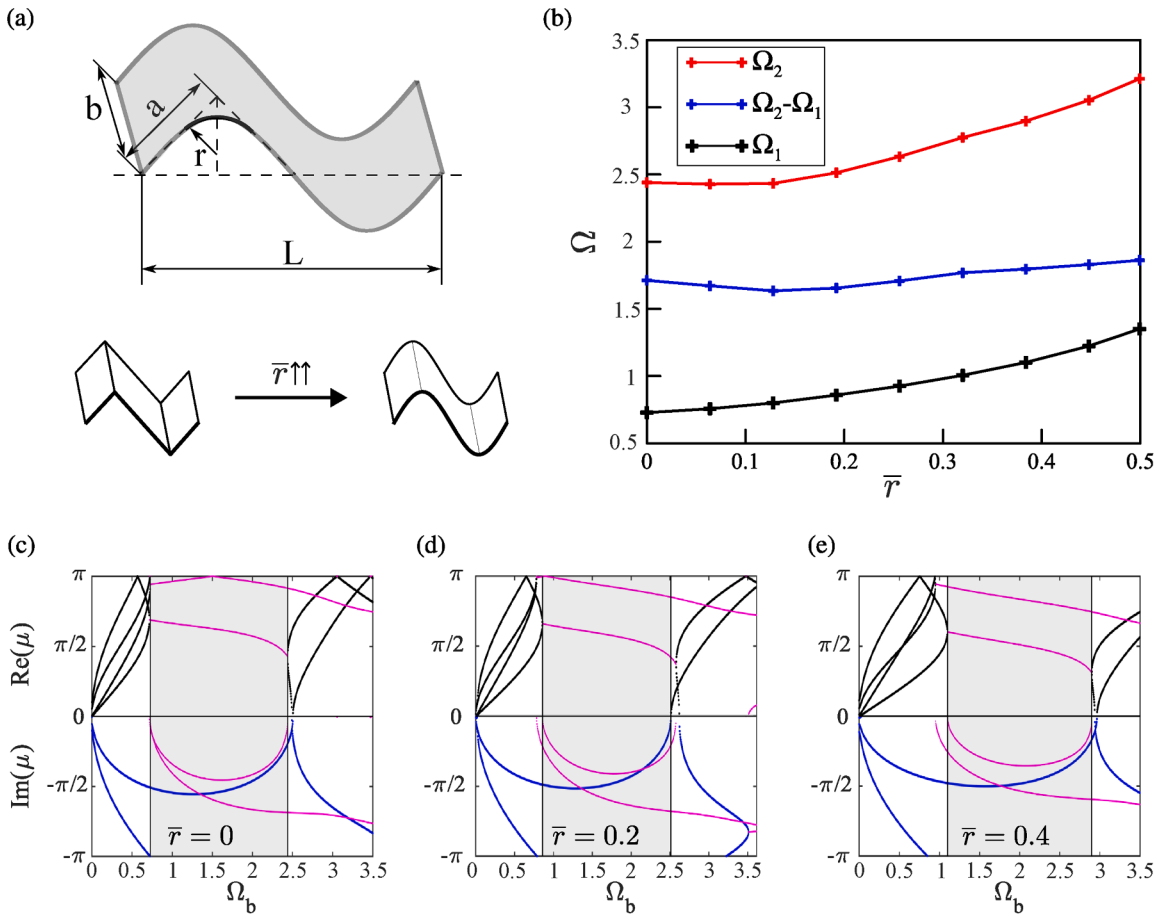

Fig. 12. Effect of crease curvature: (a) schematic figure of the unit cell; (b) evolution of the lower and upper band gap edges (Ω_1, Ω_2) and corresponding bandwidth ($\Omega_2 - \Omega_1$) as a function of $\overline{r}$; (c-e) dispersion diagrams for $\overline{r} = 0$, $\overline{r} = 0.2$, and $\overline{r} = 0.4$.

a sharp edge for the folded plates is not always guaranteed. This issue has been discussed in the modelling of origami, where methods are introduced to incorporate realistic offsets into foldable structures, e.g., [38].

To quantify the influence of finite thickness on the prediction of the first complete band gap, the dispersion characteristics of the plate strip are compared for different thickness values using two WFE models: zero-thickness shell models (four-node elements, with six DoFs per node: displacements and rotations in X,Y, and Z directions), and 3D solid models (eigth-node elements, with three DoFs per node: displacements in the X,Y, and Z directions). In the latter, thickness-induced geometric offsets are explicitly represented in the unit-cell model formulation. The same material and geometric properties described in Section 2.2 are considered. The nondimensional thickness is defined as $\overline{h} = h/a$ and varies between 0.05 and 0.2. Results are shown in Fig. 11. The nondimensional frequency, Ω_p, is evaluated using the reference frequency $\omega_{p,1}$ in Eq. (17) when $h = 0.001$ m.

The dispersion curves obtained from the shell and solid models for the thicker case ($\overline{h} = h/a = 0.2$) are presented in Fig. 11(b)-(c). The evolution of the lower and upper band edges, Ω_1 and Ω_2, and of the corresponding width of the first complete band gap with increasing $\overline{h}$ are shown in Fig. 11(d)-(f). It can be observed that, compared to the shell model, the solid model predicts a shift in the band gap edges, with the most notable difference at the lower edge. Moreover, the width of the first complete band gap increases with $\overline{h}$, which is consistent with enhanced contradirectional coupling induced by thickness effects. When thickness is included, the pair of locking wavemodes that define the lower band gap edge may change, for example, from longitudinal/flexural to torsional/flexural. This suggests that finite-thickness models can modify the hierarchy of interacting wavemodes and, consequently, the band gap topology, determining which wave family is suppressed first and enabling a more accurate band gap tuning.

The influence of crease curvature on complete band gap formation is now considered. Fig. 12(a) illustrates the unit-cell geometry, where curvature is introduced by assigning a finite crease radius defined by the nondimensional parameter $\overline{r} = r/a \in [0, 0.5]$, with $\overline{r} = 0$ representing a sharp fold. Fig. 12(c-e) show dispersion curves for $\overline{r} = 0$ and $\overline{r} = 0.2$, 0.4, while Fig. 12(b) shows the lower and upper edges of the contradirectional band gap (Ω_1, Ω_2) versus $\overline{r}$. The results show that both band gap edges shift to higher frequencies as $\overline{r}$ increases, while the overall bandwidth remains nearly constant. This behaviour can be explained considering the distributed

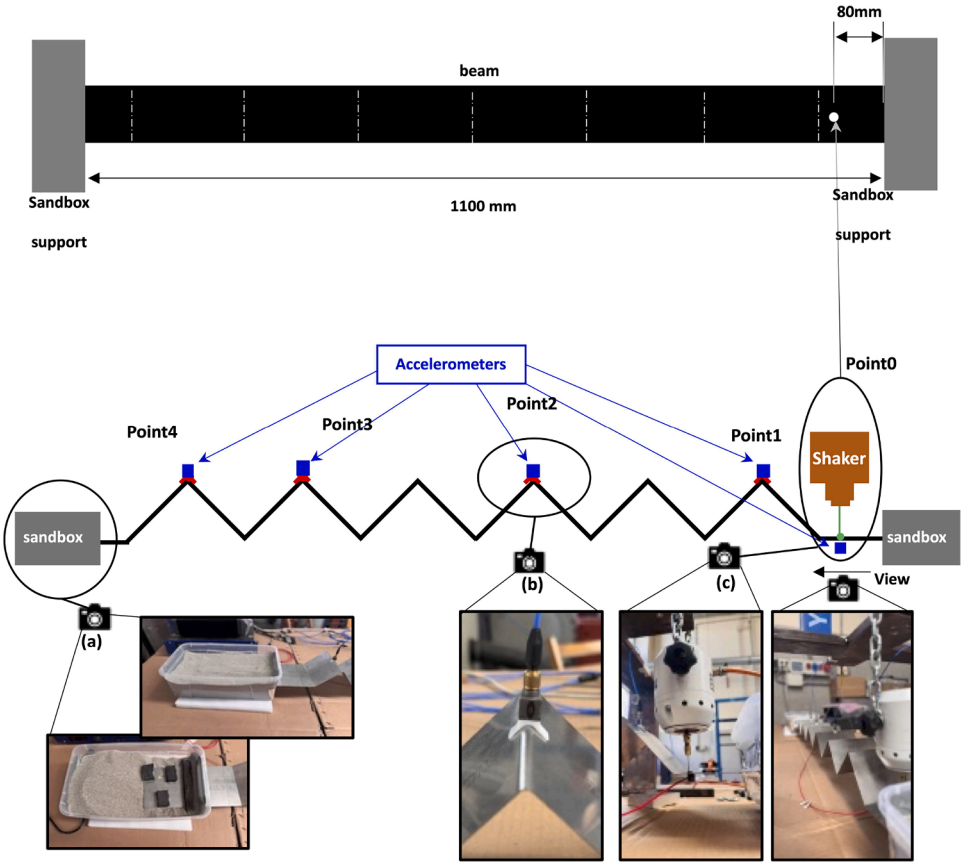

Fig. 13. Experimental setup scheme and pictures: (a) sandbox detail, (b) accelerometer details, (c) shaker and reference accelerometer detail.

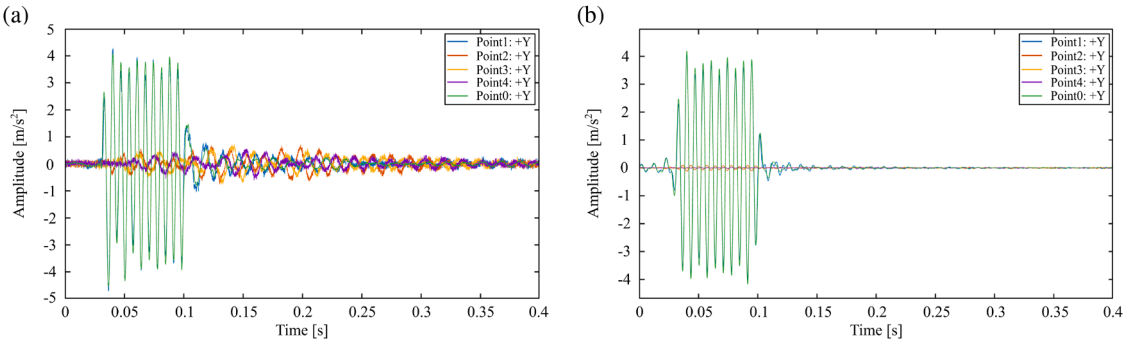

Fig. 14. Comparison between raw and filtered time histories corresponding to the 145 Hz train pulses: (a) segment of raw time history; (b) segment of filtered time history.

rotation introduced by the finite crease curvature, which modifies the local stiffness and mass distribution of the crease region but does not substantially alter the contradirectional coupling mechanism.

4. Experimental results

To validate the predicted band gap formation, experimental investigations were carried out on a finite steel plate strip with six periodically folded unit cells. The tests aimed to experimentally confirm the existence and frequency range of the complete band gap identified in the numerical analyses. The structure was subjected to controlled dynamic excitation, and the resulting vibration response was measured to extract the transmissibility, frequency response functions, wavenumber and attenuation rate. The folded plate dimensions are: $a = 0.1$ m, $b = 0.141$ m, $\alpha = 45^o$, $h = 0.8$ mm, with reference to Fig. 7. The material is steel.

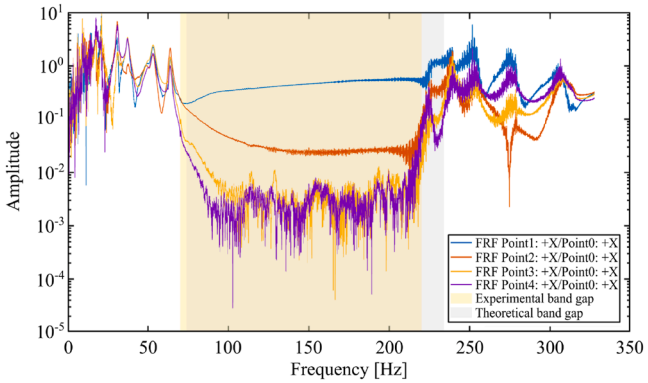

Fig. 15. Frequency response functions of measured points respect to excitation point. Yellow region: experimental band gap; grey region: WFE predicted band gap.

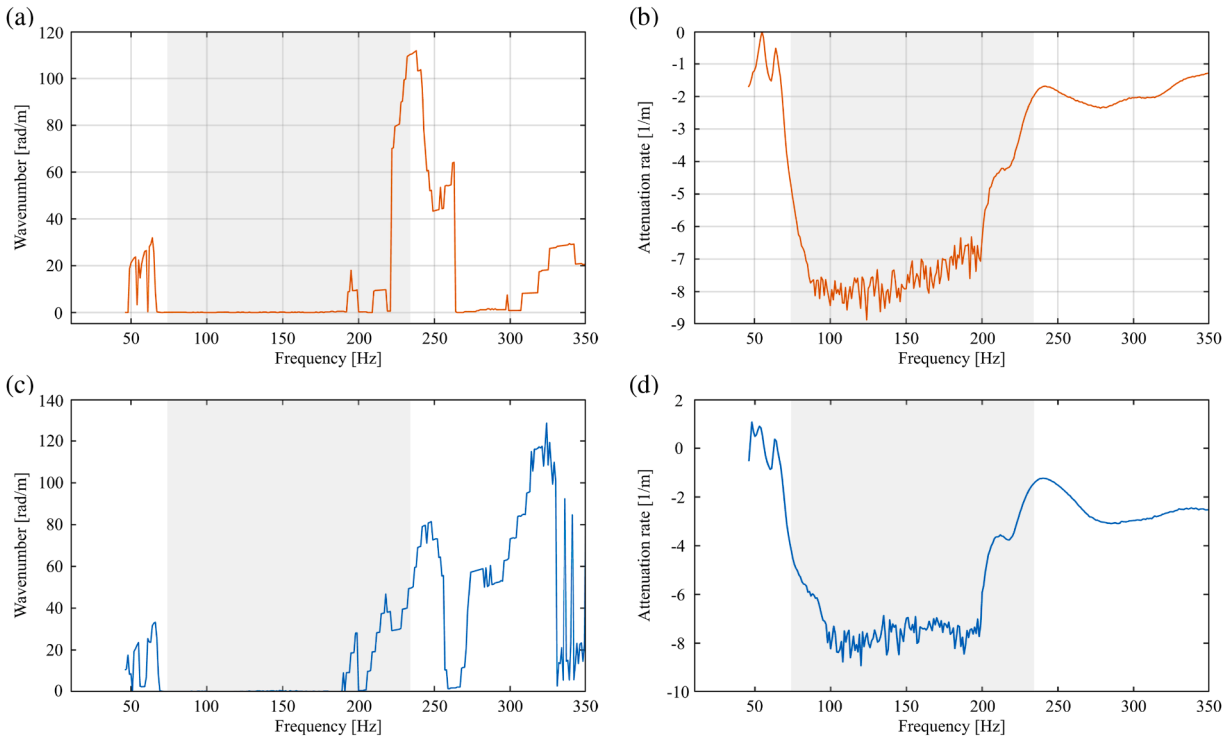

Fig. 16. Experimental wavenumber and attenuation rate: (a) wavenumber in the transverse direction; (b) attenuation rate in the transverse direction; (c) wavenumber in the axial direction; (d) attenuation rate in axial direction. Grey region: WFE predicted band gap.

Figure 13 shows the experimental setup and the periodic folded plate. The plate was positioned horizontally and supported by two sandboxes filled with dry sand. These sandboxes act as absorbent boundaries, reducing wave reflections from the boundaries; to further enhance dissipation, small foam pads were glued to the plate ends and embedded into the sand supports, Fig. 13(a). Excitation was introduced using a TIRA Vib 50,018 electrodynamic shaker, which was connected to the plate through a short stringer, orthogonally soldered to the structure. The shaker was capable of exerting a maximum force of 18 N and achieving accelerations of up to 65 g within its operational frequency range of 2 to 20000 Hz. The shaker was operated in closed-loop control using a Siemens LMS SCADAS Mobile system and TestLab software. A monoaxial accelerometer, DYTRAN3097A2, was placed under the shaker on the opposite side of the structure to capture the local input acceleration response, and four three-axial accelerometers PCB SEN041F were placed at the tips of the folded sections of the first, third, fifth, and sixth unit cells for measuring the response, Fig. 13(c). A custom 3D-printed interface ensured the correct alignment of each accelerometer with the global XYZ coordinate system, Fig. 13(b). The accelerometers were connected to the LMS SCADAS Mobile system for synchronous data acquisition, with a recorded sampling frequency of 12800 Hz. Sinusoidal pulse trains containing ten cycles per frequency were applied over the 45-500 Hz range in 2.5 Hz increments to examine the frequency response and identify attenuation bands. The acceleration data collected from the five synchronised sensors - one at the

excitation point and four on selected unit cells as in Fig. 13 - were processed using a Chebyshev digital filter to remove high-frequency noise. The filtered signals displayed a clear stopband after the third unit cell, in the frequency range predicted by the WFE [73,8 - 234,5] Hz. As an example, Fig. 14 shows the signal time histories at 145 Hz before and after filtering.

Figure 15 shows the frequency response functions (FRFs), with the experimental specimen's band gap highlighted in yellow. The figure also displays, in grey, the band gap predicted by the WFE approach (here referred to as the theoretical band gap), showing a very good agreement between the theoretical and experimental results.

The experimental evaluation of the wavenumber and attenuation along the plate, measured at point 2 (the third unit cell in Fig. 13), is presented in Fig. 16(a)-(d). In both propagation directions, the results show regions of attenuation that closely align with the theoretically predicted band gap (highlighted in grey). The attenuation bands occur in both transverse and axial directions, confirming multi-directional filtering. The good agreement between the experimental measurements and the numerical predictions supports the robustness and directional invariance of the band gap. Although real structures may exhibit geometric imperfections and nonlinear effects at sufficiently large vibration amplitudes, the measured response shows a stop band that closely aligns with the predicted frequency range (approximately 73.8-234.5 Hz; see Figs. 15-16). This indicates that, for the excitation levels adopted in the present tests, geometric nonlinearities do not appear to significantly affect the band gap edges.

5. Conclusions

This study investigated the formation of band gaps in periodically folded beams and plates, focusing on a mechanism different from Bragg scattering and local resonance effects. The complete band gaps induced by folding provide a geometry-driven, linear mechanism for broadband and directionally invariant vibration attenuation, without the need for local resonators or nonlinear stiffness effects. The findings demonstrated that the coupling between structural wavemodes propagating with opposite group velocities (contradirectional coupling) is the dominant mechanism governing the formation of complete band gaps at low frequency in periodically folded structures.

Continuous structural waveguides typically show contradirectional wave couplings in the evanescent region of the dispersion diagram. Introducing periodicity can bring this mechanism into the propagating region. At the critical points, where the dispersion branches of the corresponding periodic unfolded structure intersect in the propagating region, the wavemodes hybridise and lock under folding-induced coupling, giving rise to a complete band gap. The folding parameters govern the strength of the coupling: for small foldings the coupling is weak, and its effects are localised to the vicinity of the critical points; as the folding parameters increase, the system enters a strong-coupling regime, where the band gaps widen significantly and mode hybridisation occur. It was shown that a design process can follow a systematic sequence: identifying the reference curves of the straight periodic structure, locating the critical points, introducing folding to induce locking due to wavemodes coupling. The band gap position can then be adjusted by changing geometry, folding and material parameters, enabling tuning of a wide and robust attenuation band gap before introducing additional structural complexity.

In beams and plates structures two families of wavemodes coexist at low frequency: longitudinal-flexural and torsional-flexural. When only one family of wavemode pairs becomes locked, the remaining waves can still propagate, resulting in a partial band gap. Conversely, when both the longitudinal-flexural and torsional-flexural pairs are simultaneously locked, all propagating solutions are suppressed. This condition marks the formation of a complete band gap, within which axial, bending, and torsional vibrations are attenuated. Using the Dynamic Stiffness Method (DSM) and Wave Finite Element (WFE) formulations, it was shown how periodic folding induces longitudinal-flexural and torsional-flexural coupling in beam and plate structures. The analysis of energy and displacement fields near coupling points, supported by animations of the displacements under wave passages, showed the hybridisation and the transition mechanisms leading to the formation and disappearance of the first complete band gap.

The transition from propagating to attenuating zones was numerically analysed by evaluating the attenuation-constant-surfaces and the band-edge-surfaces, which map the space of the transfer-matrix invariants and separate regions with distinct propagation characteristics. A parametric analysis demonstrated the evolution of band edges and the transitions between propagating and attenuating zones. The results showed that the folding parameters controls the coupling strength and bandwidth in different ways according to the prescribed geometric parameters, such as the periodic lattice or the length of the folds, while modelling assumptions, such as thickness offset and fold curvature, shift the position of the predicted complete band gap and modify the hierarchy of the interacting modes, thus altering the locking-unlocking sequence and the band gap formation. These effects determine which wave family is suppressed first, showing that a proper model can enable a more accurate tuning of the complete band gap characteristics. Experimental measurements on a finite steel folded-plate validated the numerical findings, confirming the location and bandwidth of the first complete band gap.

CRediT authorship contribution statement

Elisabetta Manconi: Writing – review & editing, Writing – original draft, Validation, Software, Methodology, Formal analysis, Data curation, Conceptualization; **Filippo Dall'olio:** Writing – Original Draft, Writing - Review & Editing, Software, Formal analysis, Supervision; **Marco Riboli:** Validation, Software, Data curation; **Antonio Zippo:** Validation, Software, Formal analysis; **Farzad Tatar:** Validation, Software, Data curation.

Data availability

Data will be made available on request.

Declaration of competing interest

The authors declare that they have no known competing financial interests or personal relationships that could have appeared to influence the work reported in this paper.

Acknowledgement

This research was granted by the University of Parma through the action Bando di Ateneo 2024 per la ricerca. Part of this work was carried out while the last author was a postdoctoral fellow at the University Parma, supported by PNRR MISSION 4 COMPONENT 2 INVESTMENT 1.3 - Funded by NEXTGENERATION EU - Research program PE00000004 “Made in Italy Circolare e Sostenibile - MICS” funded by DD n.1551, 11.10.2022 on PNRR MUR - M4C2 - Investment 1.3 -“Partenariati estesi alle università, ai centri di ricerca, alle aziende per il finanziamento di progetti di ricerca di base” - D.D. n. 341, 15 marzo 2022. CUP D43C22003120001.

Supplementary material

Supplementary material associated with this article can be found in the online version at 10.1016/j.jsv.2026.119799.

Appendix A.

In this Appendix, the Dynamic Stiffness Matrix $\mathbf{D}(\boldsymbol{\omega})$ formulation of a beam in transverse and axial motion is provided. The formulation presented neglects second-order coupling between axial and bending motions. The beam is assumed as an Euler-Bernoulli beam of length L with three displacements (3 DoFs per node) corresponding to:

$$\{u_L,\ w_L,\ \theta_L,\ u_R,\ w_R,\ \theta_R\}^{\mathrm{T}},$$

where u is the axial displacement, w is the transverse displacement, and θ is the rotation at each end.

The complete dynamic stiffness matrix $\mathbf{D}$ is assembled from axial dynamic stiffness matrix $\mathbf{D}_a$ and the flexural dynamic stiffness matrix $\mathbf{D}_f$ according to Eqs. A.1 to A.5:

$$\mathbf{D} = \begin{bmatrix} \mathbf{D}_a(1,1) & 0 & 0 & \mathbf{D}_a(1,2) & 0 & 0 \\ 0 & \mathbf{D}_f(1,1) & \mathbf{D}_f(1,2) & 0 & \mathbf{D}_f(1,3) & \mathbf{D}_f(1,4) \\ 0 & \mathbf{D}_f(2,1) & \mathbf{D}_f(2,2) & 0 & \mathbf{D}_f(2,3) & \mathbf{D}_f(2,4) \\ \mathbf{D}_a(2,1) & 0 & 0 & \mathbf{D}_a(2,2) & 0 & 0 \\ 0 & \mathbf{D}_f(3,1) & \mathbf{D}_f(3,2) & 0 & \mathbf{D}_f(3,3) & \mathbf{D}_f(3,4) \\ 0 & \mathbf{D}_f(4,1) & \mathbf{D}_f(4,2) & 0 & \mathbf{D}_f(4,3) & \mathbf{D}_f(4,4) \end{bmatrix}; \tag{A.1}$$

$$\mathbf{D}_a = \frac{EAk_a}{\sin(k_aL)} \begin{bmatrix} \cos(k_aL) & -1 \\ -1 & \cos(k_aL) \end{bmatrix}, \tag{A.2}$$

where L is the segment length, A is the cross-sectional area, E is the Young’s modulus, ρ is the density, and k_a is the longitudinal wavenumber defined as $k_a = \omega\sqrt{\rho/E}$;

$$\mathbf{D}_f = \begin{bmatrix} \mathbf{D}_{f11} & \mathbf{D}_{f12} \\ \mathbf{D}_{f21} & \mathbf{D}_{f22} \end{bmatrix}, \tag{A.3}$$

where the sub-matrices $\mathbf{D}_{f11}$, $\mathbf{D}_{f12}$, $\mathbf{D}_{f21}$, $\mathbf{D}_{f22}$ are defined as:

$$\mathbf{D}_{f11} = \frac{EI}{L^3}\begin{bmatrix} \alpha & \overline{\gamma}L \\ \overline{\gamma}L & \beta L^2 \end{bmatrix}, \quad \mathbf{D}_{f12} = \mathbf{D}_{f21}^T = \frac{EI}{L^3}\begin{bmatrix} -\overline{\alpha} & \gamma L \\ -\gamma L & \overline{\beta}L^2 \end{bmatrix}, \quad \mathbf{D}_{f22} = \frac{EI}{L^3}\begin{bmatrix} \alpha & -\overline{\gamma}L \\ -\overline{\gamma}L & \beta L^2 \end{bmatrix} \tag{A.4}$$

$$
\begin{aligned}
\alpha &= \left[\cos(k_b L)\sinh(k_b L) + \sin(k_b L)\cosh(k_b L)\right]\frac{(k_b L)^3}{\Delta},\\
\overline{\alpha} &= \left[\sin(k_b L) + \sinh(k_b L)\right]\frac{(k_b L)^3}{\Delta},\\
\beta &= \left[-\cos(k_b L)\sinh(k_b L) + \sin(k_b L)\cosh(k_b L)\right]\frac{k_b L}{\Delta},\\
\overline{\beta} &= \left[-\sin(k_b L) + \sinh(k_b L)\right]\frac{k_b L}{\Delta},\\
\gamma &= \left[-\cos(k_b L) + \cosh(k_b L)\right]\frac{(k_b L)^2}{\Delta},\\
\overline{\gamma} &= \sin(k_b L)\sinh(k_b L)\frac{(k_b L)^2}{\Delta},\\
\Delta &= 1 - \cos(k_b L)\cosh(k_b L),
\end{aligned}
\tag{A.5}
$$

where I is the second moment of area of the cross-section and k_b is the flexural wavenumber defined as $k_b = \sqrt{\omega}\sqrt[4]{\left(\frac{\rho A}{EI}\right)}$.

References

[1] Z. Liu, X. Zhang, Y. Mao, Y.Y. Zhu, Z. Yang, C.T. Chan, P. Sheng, Locally resonant sonic materials, Science 289 (2000) 1734–1736. https://doi.org/10.1126/science.289.5485.1734

[2] J.H. Page, A. Sukhovich, S. Yang, M.L. Cowan, F. Van Der Biest, A. Tourin, M. Fink, Z. Liu, C.T. Chan, P. Sheng, Phononic crystals, Phys. Status Solidi B 241 (15) (2004) 3454–3462. https://doi.org/10.1002/pssb.200405363

[3] M. Miniaci, A. Gliozzi, A. Krushynska, F. Bosia, M. Scalerandi, N.M. Pugno, Proof of concept for an ultrasensitive technique to detect and localize sources of elastic nonlinearity using phononic crystals, Phys. Rev. Lett. 118 (21) (2019) 214301. https://doi.org/10.1103/PhysRevLett.118.214301

[4] J.M. De Ponti, A. Colombi, R. Ardito, F. Braghin, A. Corigliano, R.V. Craster, Graded elastic metasurface for enhanced energy harvesting, New J. Phys. 22 (1) (2020) 013013. https://doi.org/10.1088/1367-2630/ab6062

[5] R. Noroozi, M. Bodaghi, H. Jafari, A. Zolfagharian, M. Fotouhi, Shape-adaptive metastructures with variable bandgap regions by 4D printing, Polymers 12 (3) (2020). https://doi.org/10.3390/polym12030519

[6] M.I. Hussein, M.J. Leamy, M. Ruzzene, Dynamics of phononic materials and structures: historical origins, recent progress, and future outlook, Appl. Mech. Rev. 66 (4) (2014) 040802. https://doi.org/10.1115/1.4026911

[7] G. Failla, A. Marzani, A. Palermo, A.F. Russillo, D. Colquitt, Current developments in elastic and acoustic metamaterials science, Phil. Trans. R. Soc. A 382 (2269) (2024) 20230369. 10.1098/rsta.2023.0369. https://doi.org/10.1098/rsta.2023.0369

[8] D.J. Mead, Wave propagation and natural modes in periodic systems: I. Mono-coupled systems, J. Sound Vib. 40 (1) (1975) 1–18. https://doi.org/10.1016/S0022-460X(75)80227-6

[9] M.-H. Lu, L. Feng, Y.F. Chen, Phononic crystals and acoustic metamaterials, Mater. Today 12 (12) (2009) 34–42. https://doi.org/10.1016/S1369-7021(09)70315-3

[10] V. Laude, Phononic Crystals: Artificial Crystals for Sonic, Acoustic, and Elastic Waves, Walter de Gruyter GmbH & Co KG, 2020. https://doi.org/10.1515/9783110677225

[11] A. Khelif, A. Adibi, Phononic crystals, in: Springer Series in Solid-State Sciences, Springer, 2015. https://doi.org/10.1007/978-1-4614-9393-8

[12] N. Gao, Z. Wei, H. Hou, A.O. Krushynska, Design and experimental investigation of V-folded beams with acoustic black hole indentations, J. Acoust. Soc. Am. 145 (1) (2019) EL79–EL83. https://doi.org/10.1121/1.5088027

[13] P. Yeh, H.F. Taylor, Contradirectional frequency-selective couplers for guided-wave optics, Appl. Opt. 19 (16) (1980) 2848–2855. https://doi.org/10.1364/AO.19.002848

[14] W.P. Huang, Coupled-mode theory for optical waveguides: an overview, J. Opt. Soc. Am. A 11 (3) (1994) 963–983. https://doi.org/10.1364/JOSAA.11.000963

[15] L. Friis, M. Ohlrich, Coupling of flexural and longitudinal wave motion in a periodic structure with asymmetrically arranged transverse beams, J. Acoust. Soc. Am. 118 (5) (2005) 3010–3020. https://doi.org/10.1121/1.2065767

[16] B.R. Mace, E. Manconi, Wave motion and dispersion phenomena: veering, locking and strong coupling effects, J. Acoust. Soc. Am. 131 (2) (2012) 1015–1028. https://doi.org/10.1121/1.3675944

[17] E. Manconi, B. Mace, Veering and strong coupling effects in structural dynamics, J. Vib. Acoust. 139 (2) (2017) 021009. https://doi.org/10.1115/1.4035109

[18] L. Rughunanan, B. Mace, V. Sorokin, Locking and veering in periodically coupled, homogeneous waveguides and application to two coupled beams, J. Sound Vib. 630 (2026) 119699. https://doi.org/10.1016/j.jsv.2026.119699

[19] G. Trainiti, J.J. Rimoli, M. Ruzzene, Wave propagation in periodically undulated beams and plates, Int. J. Solids Struct. 75–76 (2015) 260–276. https://doi.org/10.1016/j.ijsolstr.2015.07.018

[20] J. Shi, W. Wang, Y. Fan, L. Li, C. Sbarufatti, Creating absolute band gap based on frequency locking of three wave modes in a wavy plate, J. Sound Vib. 592 (2024) 118623. https://doi.org/10.1016/j.jsv.2024.118623

[21] A. Søe-Knudsen, R. Darula, S. Sorokin, Theoretical and experimental analysis of the stop-band behavior of elastic springs with periodically discontinuous curvature, J. Acoust. Soc. Am. 132 (2) (2012) 1378–1383. https://doi.org/10.1121/1.4740480

[22] C.L. Willey, V.W. Chen, D. Roca, A. Kianfar, M.I. Hussein, A.T. Juhl, Coiled phononic crystal with periodic rotational locking: subwavelength Bragg band gaps, Phys. Rev. Appl. 18 (1) (2022) 014035. https://doi.org/10.1103/PhysRevApplied.18.014035

[23] V.F. Dal Poggetto, F. Nistri, N.M. Pugno, M. Miniaci, A.S. Gliozzi, F. Bosia, Longitudinal-flexural wave mode conversion via periodically undulated waveguides with constant and graded profiles, Phys. Rev. Appl. 24 (2025) 064050. https://doi.org/10.1103/qxr5-j641

[24] S. Tomita, T. Tachi, Tunable wave coupling in periodically rotated Miura-ori tubes, Phil. Trans. R. Soc. A 382 (2024) 20240006. https://doi.org/10.1098/rsta.2024.0006

[25] A. Nanda, M.A. Karami, Tunable bandgaps in a deployable metamaterial, J. Sound Vib. 424 (2018) 120–136. https://doi.org/10.1016/j.jsv.2018.03.015

[26] K. Bertoldi, V. Vitelli, J. Christensen, M. van Hecke, Flexible mechanical metamaterials, Nat. Rev. Mater. 2 (2017) 17066. https://doi.org/10.1038/natrevmats.2017.66

[27] H. Yasuda, J. Yang, Formation of rarefaction waves in origami-based metamaterials, Phys. Rev. E 93 (4) (2016) 043004.

[28] J.A. Faber, A.F. Arrieta, A.R. Studart, Bioinspired spring origami, Science 359 (6382) (2018) 1386–1391. https://doi.org/10.1126/science.aap7753

[29] R. Hamzehei, M. Bodaghi, N. Wu, 3D-printed multi-functional sinusoidal metamaterials for simultaneous vibration isolation and electricity generation, Eng. Struct. 345 (2025) 121496. https://doi.org/10.1016/j.engstruct.2025.121496

[30] R. Hamzehei, M. Alaei Varnosfaderani, M. Bodaghi, N. Wu, Hierarchical rotating-bending metamaterials for simultaneous mechanical vibration suppression and electricity generation, Sens. Actuators A 397 (2026) 117230. https://doi.org/10.1016/j.sna.2025.117230

[31] Z. Marciniak, J.L. Duncan, S.J. Hu, S. Jain, M. Kuzniak, J. Pawlowski, W. Szczepinski, Mechanics of Sheet Metal Forming, Butterworth-Heinemann, 1 edition, 2002. https://doi.org/10.1016/B978-0-7506-5300-8.X5000-6
[32] J.R. Banerjee, A. Ananthapuvirajah, Dynamic stiffness formulation for coupled axial-bending vibration of beams, J. Sound Vib. 331 (15) (2012) 3564–3583. https://doi.org/10.1016/j.jsv.2012.03.024
[33] J.R. Banerjee, F.W. Williams, Exact Bernoulli-Euler dynamic stiffness matrix for a range of tapered beams, Int. J. Numer. Methods Eng. 21 (12) (1985) 2289–2302. https://doi.org/10.1002/nme.1620211212
[34] J.R. Banerjee, F.W. Williams, Coupled bending-torsional dynamic stiffness matrix of an axially loaded timoshenko beam element, Int. J. Solids Struct. 31 (6) (1994) 749–762. https://doi.org/10.1016/0020-7683(94)90075-2
[35] B. Mace, D. Duhamel, M. Brennan, L. Hinke, Finite element prediction of wave motion in structural waveguides, J. Acoust. Soc. Am. 117 (2005) 2835–43. https://doi.org/10.1121/1.1887126
[36] B.R. Mace, E. Manconi, Modelling wave propagation in two-dimensional structures using finite element analysis, J. Sound Vib. 318 (4–5) (2008) 884–902. https://doi.org/10.1016/j.jsv.2008.04.023
[37] E. Manconi, B.R. Mace, R. Garziera, Wave propagation in laminated cylinders with internal fluid and residual stress, Appl. Sci. 13 (9) (2023). https://doi.org/10.3390/app13095227
[38] R.J. Lang, K.A. Tolman, E.B. Crampton, S.P. Magleby, L.L. Howell, A review of thickness-accommodation techniques in origami-Inspired engineering, Appl. Mech. Rev. 70 (1) (2018) 010805. https://doi.org/10.1115/1.4039142
[39] Y. Feng, M. Wang, X. Qiu, A simplified mechanical model of the crease in the flexible origami structures, Int. J. Solids Struct. 241 (2022) 111530. https://doi.org/10.1016/j.ijsolstr.2022.111530
[40] C.Y. Wang, Elasto-plastic folding of thin sheets, Acta Mech. 67 (1) (1987) 139–150. https://doi.org/10.1007/BF01182128
[41] E. Nolde, A.V. Pichugin, J. Kaplunov, An asymptotic higher-order theory for rectangular beams, Proc. R. Soc. A Math. Phys. Eng. Sci. 474 (2210) (2018) 20180001. https://doi.org/10.1098/rspa.2018.0001
[42] T.M. Wang, T.A. Kinsman, Vibrations of frame structures according to the Timoshenko theory, J. Sound Vib. 14 (2) (1971) 215–227. https://doi.org/10.1016/0022-460X(71)90385-3
[43] D.J. Mead, Wave propagation and natural modes in periodic systems: II. multi-coupled systems, with and without damping, J. Sound Vib. 40 (1) (1975) 19–39. https://doi.org/10.1016/S0022-460X(75)80228-8
[44] Y. Xiao, B.R. Mace, J. Wen, X. Wen, Formation and coupling of band gaps in a locally resonant elastic system comprising a string with attached resonators, Phys. Lett. A 375 (12) (2011) 1485–1491. https://doi.org/10.1016/j.physleta.2011.02.044
[45] F. Romeo, A. Paolone, Wave propagation in three-coupled periodic structures, J. Sound Vib. 301 (3) (2007) 635–648. https://doi.org/10.1016/j.jsv.2006.10.017